



저작자표시-비영리-변경금지 2.0 대한민국

이용자는 아래의 조건을 따르는 경우에 한하여 자유롭게

- 이 저작물을 복제, 배포, 전송, 전시, 공연 및 방송할 수 있습니다.

다음과 같은 조건을 따라야 합니다:



저작자표시. 귀하는 원저작자를 표시하여야 합니다.



비영리. 귀하는 이 저작물을 영리 목적으로 이용할 수 없습니다.



변경금지. 귀하는 이 저작물을 개작, 변형 또는 가공할 수 없습니다.

- 귀하는, 이 저작물의 재이용이나 배포의 경우, 이 저작물에 적용된 이용허락조건을 명확하게 나타내어야 합니다.
- 저작권자로부터 별도의 허가를 받으면 이러한 조건들은 적용되지 않습니다.

저작권법에 따른 이용자의 권리는 위의 내용에 의하여 영향을 받지 않습니다.

이것은 [이용허락규약\(Legal Code\)](#)을 이해하기 쉽게 요약한 것입니다.

[Disclaimer](#)

이학박사학위논문

Top-down estimates of soil dust emissions
in East Asia using inverse methods

인버스 기법을 이용한 동아시아 먼지 에어로졸의
위에서 아래로의 배출량 산정

2012년 8월

서울대학교 대학원

지구환경과학부

구 본 양

인버스 기법을 이용한 동아시아 먼지
에어로졸의 위에서 아래로의 배출량 산정
Top-down estimates of soil dust emissions in
East Asia using inverse methods

지도교수 박 록 진

이 논문을 이학박사 학위논문으로 제출함
2012년 4월

서울대학교 대학원
지구환경과학부
구 본 양

구본양의 이학박사 학위논문을 인준함
2012년 6월

위 원 장 _____ (인)

부위원장 _____ (인)

위 원 _____ (인)

위 원 _____ (인)

위 원 _____ (인)

ABSTRACT

Soil dust is the dominant aerosol by mass concentration in the troposphere and has considerable effects on air quality and climate. Parts of East Asia, including Southern Mongolia, Northern China, and the Taklamakan Desert, are important dust source regions. Accurate simulations of dust storm events are crucial for protecting human health and assessing the climatic impacts of dust events. However, even state-of-the-art aerosol models still contain large uncertainties in soil dust simulations, particularly for the dust emissions over East Asia. This study attempts to reduce these uncertainties by using an inverse modeling technique to simulate dust emissions, and obtain optimized estimates of soil dust sources in East Asia. The global three-dimensional GEOS-Chem chemical transport model (CTM) is used as a forward model to simulate the mass concentrations of particles less than $10\ \mu\text{m}$ in aerodynamic diameter (PM_{10}) including non-dust in addition to dust aerosols during springtime focusing on April 2001 (period 1) and May 2007 (period 2). I use observation data including ground-based PM_{10} mass concentrations and satellite Moderate Resolution Imaging Spectrometer (MODIS) aerosol optical depths (AODs) over East Asia to evaluate the model. The inverse model analyses are also used to compare the top-down estimates of dust emissions using daily MODIS AODs and PM_{10}

concentrations in the surface air. The model error is large over dust source regions including the Gobi Desert and Mongolia. The inverse modeling analyses from the MODIS AODs and PM₁₀ observations consistently result in decrease of dust emissions over Mongolia and the Gobi Desert and the simulation results with the a posteriori dust sources show much better agreement with observations. This study presents that the inverse modeling technique can be useful for estimation of the optimized dust emissions from individually sourced regions. Whereas over the Taklamakan Desert and Manchuria, the inverse modeling analyses from both observations yield contrast results such as increase of dust sources using MODIS AODs, but decrease of those using PM₁₀ observations. In this study, some limitations of both observations to obtain the optimized dust emissions are discussed and several strategies for the improvement of dust emission estimates in the model are suggested based on the inverse modeling analyses.

Keywords: Inverse modeling, Dust emission, Chemical transport model (CTM), Particulate matter (PM₁₀), Aerosol optical depth (AOD)

Student Number: 2000-30258

TABLE OF CONTENTS

ABSTRACT	i
TABLE OF CONTENTS	iii
LIST OF FIGURES	v
LIST OF TABLES	x
CHAPTER I	
INTRODUCTION	1
1.1. Background and motivation	1
1.2. Objective of the thesis	4
CHAPTER II	
Data and methodology	6
2.1. Forward model	6
2.2. Observations	12
2.2.1. Ground-based PM ₁₀ mass concentration	12
2.2.2. Satellite Aerosol optical depth (AOD)	15
2.3. Inverse model	20
2.3.1. Description	20
2.3.2. Error specification	23
CHAPTER III	
Model evaluation with a priori dust sources	28
3.1. Simulation of dust events in April 2001 (period 1)	28
3.2. Simulation of dust events in May 2007 (period 2)	35

CHAPTER IV	
Inverse modeling analysis of dust sources during the period 1	43
4.1. A posteriori dust sources from PM ₁₀ observations	43
4.2. Issues with the inverse modeling analysis of dust emissions	56
CHAPTER V	
Comparative inverse analysis of MODIS AODs and PM₁₀ observations to estimate dust emissions during the period 2	60
5.1. A posteriori dust sources from PM ₁₀ observations	64
5.2. Comparative analysis of a posteriori dust sources from MODIS AODs	68
CHAPTER VI	
Improvement of dust emission simulations in the model	79
CHAPTER VII	
Summary and conclusions	86
REFERENCES	90
국문 초록	100

LIST OF FIGURES

- Figure 2.1. Dust source regions are divided into 10 source areas (S1 to S10 indicated with black dashed line boxes) and the rest of the world (RoW). Locations of PM₁₀ observation sites in China (n=26), Korea (n=133), and Japan (n=10) are denoted with yellow squares, red dots, and blue triangles, respectively. AEROSOL ROBOTIC NETWORK (AERONET) sites (n=11) are indicated with black stars. Grey square shows the area for the used Moderate Resolution Imaging Spectrometer (MODIS) aerosol optical depth (AOD) data. 10
- Figure 2.2. Scatterplots of AERONET versus MODIS/Aqua AODs. The 11 AERONET sites in East Asia are used during the period of 2006 to 2010 and the AERONET AODs are averaged around the overpass time of the AQUA platform over East Asia (1:30 PM). The horizontal resolution of MODIS AODs is regridded to 2°x2.5° for comparison to the model. The dashed lines indicate the 2:1, 1:1, and 1:2 lines. 19
- Figure 2.3. Model error variance for the MODIS AOD data in May 2007 using GEOS-Chem as a forward model during 00-07 UTC for the satellite overpass time in East Asia. White areas indicate missing data. 25
- Figure 3.1. Observed daily PM₁₀ concentrations versus modeled PM₁₀ concentrations with the a priori emissions at Huhehaote, Zhenzhou, Dalian, and Yantai in China from 1 April to 10 May in 2001. Black dots show observations and colored bars show simulated concentrations. Different colors indicate the individual contributions of dust aerosols from each source region; non-dust aerosols are shown in white. 30

Figure 3.2. Same as in Fig. 3.1 but at Seoul, Incheon, Daejeon, and Busan in Korea.	31
Figure 3.3. Same as in Fig. 3.1 but at Oki, Ijira, Yusuhara, and Banryu in Japan.	32
Figure 3.4. Modeled column concentrations of dust aerosols with a priori sources and SYNOP dust code (S) from 21 to 28 May in 2007. The red colored S represents blowing sand (code #7, 8) and dust storm (code #9, 30, 31, 32, 33, 34, 35, 98) and the blue colored S indicates floating dust (code #6).	36
Figure 3.5. Daily MODIS AODs versus modeled AODs with a priori sources from 21 to 28 May in 2007. The horizontal resolution of MODIS data is regridded to $2^{\circ} \times 2.5^{\circ}$ and white areas indicate missing data.	38
Figure 3.6. Observed daily PM_{10} concentrations versus modeled PM_{10} concentrations with the a priori emissions at Shanghai and Dalian in China, Baengnyeongdo and Kwanaksan in Korea for May 2007.....	40
Figure 3.7. Scatterplots of the observed versus simulated PM_{10} mass concentrations with a priori dust sources at China, Korea, and Japan in May 2007.....	42
Figure 4.1. Simulated dust emissions (upper) and surface air dust concentrations (lower) of the a priori (left) and a posteriori dust sources (right).....	44
Figure 4.2. Observed daily PM_{10} concentrations versus modeled PM_{10} concentrations with the a priori emissions (left) and the a posteriori emissions (right) at Huhehaote, Zhenzhou, Dalian, and Yantai in China.	48
Figure 4.3. Same as in Fig. 4.2 but at Seoul, Incheon, Daejeon, and Busan in Korea.	49

Figure 4.4. Same as in Fig. 4.2 but at Oki, Ijira, Yusuhara, and Banryu in Japan.	50
Figure 4.5. Aerosol Index (AI) from Total Ozone Mapping Spectrometry (TOMS) versus modeled column concentrations of black carbon and dust aerosols with the a priori and a posteriori dust sources in April 2001. The horizontal resolutions of TOMS AI and model simulations are $1.0^{\circ} \times 1.25^{\circ}$ and $2.0^{\circ} \times 2.5^{\circ}$, respectively.....	52
Figure 4.6. Monthly mean AODs from the Multi-angle Imaging Spectrometer (MISR) versus model values from the a priori and a posteriori sources in April 2001. The horizontal resolution of MISR data is $0.5^{\circ} \times 0.5^{\circ}$ and white areas indicate missing data. Note the difference in color scales.....	54
Figure 4.7. Estimates of dust emissions for each source region from inverse modeling analyses. Values with a priori source are forward model results and a posteriori is the best estimates in this study. Each case shows the sensitivity results using different errors and data selections. Cases 1 and 2 show results with 1% and 50% instrumental errors, respectively, and cases 3 and 4 are derived with 150% and 250% errors, respectively, for dust sources using all PM_{10} observations from China, Korea, and Japan. Case 5 is the result from assigning different transport errors of 100%, 30%, and 70% for China, Korea, and Japan. Cases 6–8 are obtained with 200% dust source errors and 93% transport error and with different data selections. The data for case 6 include the PM_{10} observations from China alone. In cases 7 and 8, the PM_{10} observations above $50 \mu\text{g m}^{-3}$ and $100 \mu\text{g m}^{-3}$, respectively, from China, Korea, and Japan are used.	58
Figure 5.1. Simulated dust emissions with (a) a priori, (b) a posteriori from PM_{10} concentrations, and (c) a posteriori from MODIS Deep Blue AODs.....	61

- Figure 5.2. Observed daily PM_{10} concentrations versus modeled PM_{10} concentrations with the a priori emissions (left), the a posteriori emissions from the PM_{10} observations (middle), and the a posteriori emissions from the MODIS Deep Blue AODs (right) at Shanghai and Dalian in China, Baengnyeongdo and Kwanaksan in Korea for May 2007.....65
- Figure 5.3. Scatterplots of the observed versus simulated PM_{10} mass concentrations with (a-c) a priori dust sources and with (d-f) a posteriori dust sources from the PM_{10} observations at China, Korea, and Japan in May 2007.67
- Figure 5.4. GEOS-Chem model mean bias in the simulation of AODs with (a) a priori sources, (b) a posteriori sources from the PM_{10} concentrations, and (c) a posteriori sources from the MODIS Deep Blue AODs. The bias is defined as the mean of the difference between simulated and observed AODs averaged in May 2007..... 73
- Figure 5.5. Monthly mean UV Aerosol Index (AI) from the Ozone Monitoring Instrument (OMI) versus modeled column concentrations of black carbon and dust aerosols with the a priori and a posteriori dust sources from the PM_{10} observations and the MODIS Deep Blue AOD measurements in May 2007. The horizontal resolutions of TOMS AI and model simulations are $1^{\circ}\times 1^{\circ}$ and $2^{\circ}\times 2.5^{\circ}$, respectively. Note the difference in color scales.75
- Figure 5.6. Estimates of dust emissions for the dominant individual source regions (S2-S6, S8) from the inverse modeling analyses. Values with the a priori sources are the forward model results and those with the a posteriori sources are the optimized estimates from the MODIS Deep Blue AOD measurements. Each case shows sensitivity results using different data selections. This study uses the MODIS Deep Blue AODs data only in the

source regions from S1 to S8. Case 1-3 include the MODIS Deep Blue AODs data in the source regions from S1 to S9, from S1 to S10, and in the domain 21-51°N, 71-146°E including downwind regions as well as source regions, respectively..... 77

Figure 6.1. Vertical dust flux as a function of friction velocity (a) for the different clay mass fraction from 0.1 to 0.3 and (b) for the source function from 0.2 to 0.6 in the model. 80

Figure 6.2. Simulated dust emissions with (a) the a priori, (b) using variable clay mass fractions with 0.2 cap, (c) the a posteriori from PM₁₀ concentrations, and (d) the a posteriori from MODIS AODs in May 2007. 82

Figure 6.3. Scatterplots of the observed versus simulated PM₁₀ mass concentrations with (a) the a priori, (b) using variable clay mass fractions with 0.2 cap, (c) the a posteriori from PM₁₀ concentrations, and (d) the a posteriori from MODIS AODs in May 2007. 83

LIST OF TABLES

Table 2.1. National Standard of the Ambient Air Quality in China.....	14
Table 4.1. Inverse modeling analysis of dust sources over East Asia in the domain 10–60°N, 70–150°E for April 2001.....	46
Table 5.1. Inverse modeling analysis of dust sources over East Asia in the domain 10–60°N, 70–150°E for May 2007.	62

CHAPTER I

INTRODUCTION

1.1. Background and motivation

Soil dust aerosols are the largest contributor to aerosol mass concentrations in the troposphere (Forster et al., 2007) and influence global climate by affecting the radiation budget (Sokolik and Toon, 1996) and biogeochemical cycling (Jickells et al., 2005). In addition, soil dust aerosols play an important role in atmospheric chemistry by providing a surface area for heterogeneous reactions. The resulting poor air quality can lead to problems ranging from degraded visibility to respiratory illnesses (Kwon et al., 2002; Prospero, 1999). As the influence of dust aerosols on the global environment is increasingly recognized, there is a growing need for an accurate quantification of dust aerosol concentrations and thus its emissions in source regions.

Dust aerosols are naturally produced by wind erosion of the Earth's crust, a complicated process affected by numerous meteorological and surface conditions including surface wind speed, friction velocity, soil temperature, soil moisture, soil texture, landuse type, and snow and vegetation cover (Kurosaki and Mikami,

2004). Among the many dust source regions in arid and semi-arid areas, the Sahara Desert in North Africa is the most important, contributing 50-70% of annual global soil dust aerosol emissions (Tanaka and Chiba, 2006).

East Asia is also an important source region, accounting for 3-11% of global dust emissions (Tanaka and Chiba, 2006). More importantly, the dust source regions in East Asia are close to populated areas. East Asian dust storm outbreaks are common in spring over Mongolia and the Taklamakan and Gobi deserts and can result in substantial economic losses and environmental damage (Seinfeld et al., 2004). Dust aerosols emitted from East Asia are usually trapped and transported within the planetary boundary layer and affect regional air quality. Occasionally they are elevated to the free atmosphere, and with favorable meteorological conditions, reach thousands of kilometers to North America (Hsu et al., 2006; Zhao et al., 2008), thereby dust aerosols from East Asia are even important on a hemispheric scale.

In the context of air quality, it is crucial to understand dust mobilization that has been investigated with observations in dust source regions as well as numerical simulations. Especially, numerical models are important tools to test the theoretical scientific understanding learned from the observations and can further be applied for other uses. Previous studies have applied three-dimensional (3-D) regional air quality models to simulate dust aerosols over East

Asia (Gong et al., 2003; Park and In, 2003; Uno et al., 2003). A dust model inter-comparison (DMIP) study examined the current regional dust models applied to the Asian domain (Uno et al., 2006) and concluded that the dust aerosol transport patterns from the source regions were usually very similar, while the simulated dust concentrations in the surface air sometimes differed by over two orders of magnitude in the dust source regions. The simulation discrepancies are mainly attributable to uncertainties in the dust emission simulations, which are typically parameterized by wind speed, soil water content, and vegetation cover (Marticorena and Bergametti, 1995; Tegen and Fung, 1994). Reducing these uncertainties and accurately quantifying dust emissions are critical for improving dust model capabilities.

Data assimilation is a noble method of combining observations into the numerical simulation, is effective to tackle manifest issues of numerical models related to initial conditions and boundary conditions, and provides insights into the underlying issues that can be used to enhance the modeling capability. It has been applied to the chemical transport model simulations: black carbon aerosol by Hakami et al. (2005); carbon monoxide by Kopacz et al. (2009); ozone by Zhang et al. (2009); inorganic aerosols by Henze et al. (2009). Recently state-of-the-art data assimilation methods such as the ensemble Kalman filter (EnKF) and the four-dimensional variational method (4D-Var) have been applied to dust

aerosol models using ground-based and satellite optical observations to optimize dust emissions in the model (Sekiyama et al., 2010; Wang et al., 2012; Yumimoto et al., 2008).

1.2. Objective of the thesis

The objective of this study is to obtain the optimized estimates of soil dust sources in East Asia, then to examine the factors affecting dust emissions. That information is used to enhance our understanding of dust mobilization that can reduce uncertainties of dust emission estimates in the model.

For this, a relative common analytical method for solving a Bayesian inverse problem is applied to constrain soil dust sources in East Asia. The inverse model is a standard tool for combining observations of atmospheric composition with simulations for its atmospheric processes (transport, chemistry, deposition) to derive quantitative constraints on emissions to the atmosphere. I used observations including Moderate Resolution Imaging Spectrometer (MODIS) aerosol optical depths (AODs) and ground-based mass concentrations of particles less than 10 μm in aerodynamic diameter (PM_{10}) observations over East Asia. This study examines the robustness of the inverse model and some limitations of different observations used for the optimization of dust emissions.

Based on the inverse modeling analysis, this study finally suggests some strategies for the improvement of dust emission estimates in the model.

CHAPTER II

Data and methodology

2.1. Forward model

A global 3-D chemical transport model (GEOS-Chem) is used to conduct aerosol simulations, including of dust aerosol over East Asia (Fairlie et al., 2007; Park et al., 2004). The model (v.8.1.1, <http://acmg.seas.harvard.edu/geos/>) has a horizontal resolution of 2° latitude \times 2.5° longitude with 30 vertical levels from the surface to 0.01 hPa and is driven by assimilated meteorological data from the Goddard Earth Observing System (GEOS) of the NASA Global Modeling and Assimilation Office (GMAO). I used GEOS-3 and GEOS-5 meteorology fields to conduct aerosol simulations. The GEOS-Chem was applied for an intercomparison study of CTM simulations of CO during the Transport and Chemical Evolution over the Pacific mission period and showed no bias in GEOS-Chem transport driven by GEOS-3 assimilated meteorological data (Kiley et al., 2003). Aerosol simulations in GEOS-Chem have been described in detail elsewhere (Fairlie et al., 2007; Park et al., 2004; Park et al., 2006).

For soil dust mobilization, this study uses the dust entrainment and deposition (DEAD) scheme of Zender et al. (2003) combined with the source function used in GOCART (Ginoux et al., 2001), as described in Fairlie et al. (2007). That scheme treats the vertical dust flux (F) as proportional to the horizontal saltation dust flux (Q_s) that is computed following Marticorena and Bergametti (1995) based on the theory of White (1979) as in the following.

$$Q_s = C_z \frac{\rho_{air}}{g} U^{*3} \left(1 - \frac{U_t^*}{U^*}\right) \left(1 + \frac{U_t^*}{U^*}\right)^2 \quad (2.1)$$

where U^* is the friction velocity U_t^* is the threshold friction velocity, ρ_{air} is the air density, g is the acceleration of gravity. Here the friction velocity is computed using the 10m wind speed assuming neutral stability and variations in threshold friction velocity for different soil properties are not considered. The total vertical dust flux (F) is given by

$$F = (1 - A_s) S \alpha Q_s \quad (2.2)$$

where A_s is the fraction of snow-covered ground, S is the source function that confines dust emissions to topographic depressions in desert and semi-desert areas of the world, and α is the sandblasting mass efficiency depending on the mass fraction of clay in the soil. In the model the mass fraction of clay particles in the parent soil is assumed to be constant that might possess nontrivial

uncertainty. In addition, the threshold friction velocity, at which soil particles begin to be mobilized, is assigned to be a fixed value for smooth dry surface. Although the impact of soil moisture on the threshold friction velocity is taken into account with a correction factor, possible errors can be caused by the present approach adding some uncertainties to dust mobilization in the model. Size-segregated dust aerosols are computed using the tri-modal lognormal probability density function that is arranged into four size bins (radii 0.1–1.0, 1.0–1.8, 1.8–3.0, and 3.0–6.0 μm).

The forest fire aerosol sources in the model are calculated by multiplying the burned areas by emission factors dependent on the species and vegetation types from Andreae and Merlet (2001). The burned areas data are from the Global Fire Emission Database version 2 (GFEDv2; van der Werf et al., 2006) which is derived using MODIS fire count observations to determine the locations and periods of active fire hot spots (Giglio et al., 2006) and has a spatial resolution of $1^\circ \times 1^\circ$ and monthly temporal resolution.

The dry deposition of dust aerosol is represented with a deposition velocity that is defined by the gravitational settling and turbulent transfer of particles to the surface (Seinfeld and Pandis, 1998; Zhang et al., 2001). The wet deposition process for dust aerosol includes scavenging in convective updrafts and rainout

and washout from large-scale precipitation and convective anvils (Liu et al., 2001).

The major source regions of soil dust aerosols over Asia include the deserts in Mongolia and Western and Northern China, including the Taklamakan and Gobi deserts. Other arid regions in Northeastern China and Inner Mongolia have become important soil dust sources as desertification and deforestation progress along with industrialization and climate changes (Chin et al., 2003; Lim and Chun, 2006). To quantify the dust source contributions from different source regions, tagged dust aerosol simulations that carry separate dust aerosol tracers from individual source regions (Zhang et al., 2003b) are conducted. The model computes the dust concentrations, which are calculated with geographically separated dust emissions from 11 dust source regions as shown in Fig. 2.1. These include the deserts and sands in Kazakhstan (S1), the Mongolian Plateau (S2), the Taklamakan Desert (S3), the Tsaidam basin and Kumutage Desert (S4), the Badan Jaran, Tengger, and Ulan Buh deserts (S5), the Mu Us and Hobq deserts (S6), the Onqin Dega sandy land (S7), the Horqin sandy land (S8), historical deposition areas (S9 and S10), and the rest of the world (RoW).

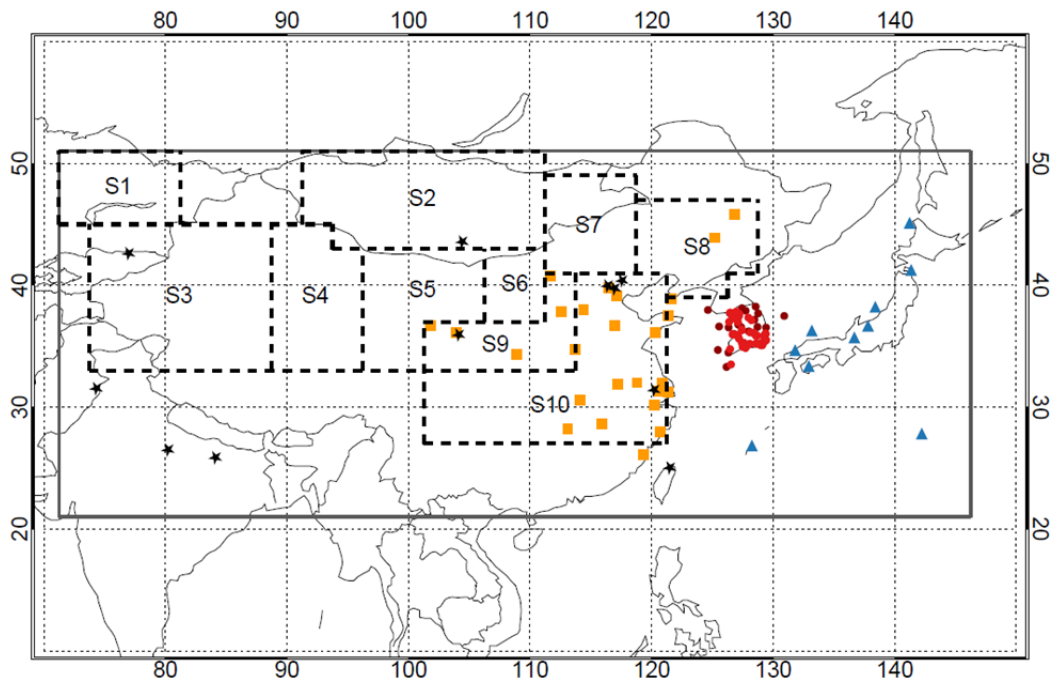


Figure 2.1. Dust source regions are divided into 10 source areas (S1 to S10 indicated with black dashed line boxes) and the rest of the world (RoW). Locations of PM_{10} observation sites in China (n=26), Korea (n=133), and Japan (n=10) are denoted with yellow squares, red dots, and blue triangles, respectively. AERONET sites (n=11) are indicated with black stars. Grey square shows the area for the used Moderate Resolution Imaging Spectrometer (MODIS) aerosol optical depth (AOD) data.

Forward model simulations are conducted for the tagged dust aerosols and non-dust aerosols from January to May 2001 with the GEOS-3 meteorological data and from January to May 2007 with the GEOS-5 meteorological data. This study primarily focuses on April 2001 (hereafter referred to as period 1) and May 2007 (hereafter referred to as period 2) when intense dust storms occurred and affected East Asia.

2.2. Observations

2.2.1. Ground-based PM₁₀ mass concentration

Daily observations of PM₁₀ mass concentrations in the surface air over East Asia are used to evaluate the model simulations and estimate the optimized dust emissions. The observed PM₁₀ mass concentrations are measured with automatic instruments using the β -ray absorption method and the Tapered Element Oscillating Microbalance method in China as well as Korea and Japan. The used PM₁₀ concentrations are quantitative measures for uniformly monitoring mass concentrations of particles less than 10 μm in aerodynamic diameter in the surface air. These instruments errors for particulate matter measures are 2-9%, which are relatively small to the total temporal variability (Goldman et al., 2009). The data are obtained from the Chinese Ministry of Environmental Protection (MEP, formerly SEPA, <http://datacenter.mep.gov.cn>), the Korean Ministry of Environment (MOE, <http://www.airkorea.or.kr>), the Korea Meteorological Administration (KMA, <http://www.kma.go.kr>) and the Acid Deposition Monitoring Network (EANET, <http://www.eanet.cc>) in Japan.

The observed PM₁₀ concentrations over China are derived from the ambient air pollution index (API), which is a semi-quantitative measure, designed to

uniformly report the air quality in China (see Table 2.1). At each observational site, the concentrations of PM₁₀, SO₂, and NO₂ are automatically measured and a corresponding API value is reported as a dimensionless number from 0 to 500 for the highest pollutant concentration on a given day. The pollutant type on a given day is also inferred, except for “clean” days when the API value is below 50 (i.e., the concentrations of NO₂, SO₂, and PM₁₀ are below 80, 50, and 50 $\mu\text{g m}^{-3}$, respectively). Here only the PM₁₀-polluted days and clean days are considered. Details on the API data and calculation of PM₁₀ concentrations from APIs can be found in previous studies (Choi et al., 2009; Gong et al., 2007; Zhang et al., 2003a). The PM₁₀ concentrations converted from APIs in China are associated with dust storm propagation (Chu et al., 2008). The available 26 Chinese observation sites are located in Central-eastern China (east of 100°E) and are affected by dust outbreaks in spring.

Table 2.1. National Standard of the Ambient Air Quality in China.

API	Daily mean concentrations ($\mu\text{g m}^{-3}$)		
	SO ₂	NO ₂	PM ₁₀
50	50	80	50
100	150	120	150
200	800	280	350
300	1600	565	420
400	2100	750	500
500	2620	940	600

In Korea, PM₁₀ concentrations are routinely observed across the country. The observed daily PM₁₀ mass concentrations were available at 133 sites in Korea. The majority of sites are in urban areas. The Korean government releases quality-assured (QA) and quality-controlled (QC) data in which abnormal values are filtered out through the data screening process.

The EANET project was initiated to improve our understanding of the acid deposition problem in East Asia. Since January 2001, regular measurements of aerosol species concentrations have been conducted, including measurements of gaseous pollutants, soluble aerosols, and PM₁₀. The used daily PM₁₀ concentrations are from 10 EANET sites in Japan. These sites are mainly located on islands and in rural and mountainous regions to avoid the direct influence of a local source. All the observed PM₁₀ concentrations discussed above are averaged over the corresponding 2°×2.5° horizontal grids to estimate dust emissions and compare with the model.

2.2.2. Satellite Aerosol optical depth (AOD)

The Moderate Resolution Imaging Spectrometer (MODIS) is one of the sensors on board EOS-AM1/Terra and EOS-PM1/Aqua, which are both sunsynchronous polar orbiting satellites. Terra was launched on Dec. 12, 1999

and flies northward pass the equator at about local time 10:30 AM. Aqua, launched on May 4, 2002, flies southward pass the equator at about local time 1:30 PM. The time interval of their overpass at the same area is usually less than 3 hours (Tang et al., 2005). MODIS observations provide continuous data for AODs over East Asia with near-complete spatial coverage every day, limited by cloud cover. Here I use AODs at 550 nm in the MODIS/Aqua Level-3 (MYD08) daily gridded atmospheric products (Optical_Depth_Land_And_Ocean_Mean), which are derived from the statistics of the Level 2 products and stored on a $1^{\circ} \times 1^{\circ}$ equal-angle grid in the MYD08 Level-3 product file. Reported uncertainties of MODIS AODs over land are $0.05 \pm 15\%$ (Chu et al., 2002; Ichoku et al., 2005; Remer et al., 2005) with higher errors over snow covered areas, arid regions and coastal regions (Abdou et al., 2005) in that MODIS cannot adequately measure the solar reflectance of surfaces with such high albedo. Retrieving aerosol properties over dust source regions is a difficult task using traditional Advanced Very High Resolution Radiometer (AVHRR) channels in the visible and near-infrared wavelengths due to the bright underlying surfaces of arid and semi-arid areas.

Therefore I choose other MODIS/Aqua AOD products (Deep_Blue_Aerosol_Optical_Depth_550_Land_QA_Mean), which are obtained with the Deep Blue algorithm (Hsu et al., 2004) that is the optimal method for retrieving aerosols

over high-reflectance arid and semi-arid areas. The Deep Blue algorithm employs radiances from the blue channels (412 nm) of the MODIS/Aqua instrument, where surface reflectance is low enough to make such retrievals possible. The Deep Blue retrieval provides AODs over bright surfaces including deserts where the dominant aerosol type is dust. For the inverse modeling, the Deep Blue AODs at 550 nm are used in order to provide AODs observations over the arid and semi-arid regions where the standard MODIS AOD data are not available.

For the model evaluation, the composite AODs of two products described above are used for the purpose of increasing spatial coverage in East Asia. The composite AODs are obtained by averaging two AOD data at 550 nm arithmetically in grids where above two products are available, otherwise available AOD products are selected in each grid, and then they are regridded to $2^{\circ} \times 2.5^{\circ}$ horizontal resolution for a comparison with the model.

To evaluate the MODIS/Aqua composite AODs at 550 nm, the observed AODs from the 11 AERosol RObotic NETwork (AERONET) sites in East Asia (site locations are shown with black stars in Fig. 2.1) are used. AERONET is a network of automated sun/sky radiometers, which measures the attenuation of direct sunlight at near-infrared and visible wavelengths (1020, 935, 870, 675, 500, 440, 380 and 340 nm) to derive the corresponding aerosol optical depths

and the Angström exponent between a number of wavelength pairs (440-870, 380-500, 440-675, 500-870, and 340-440 nm; Holben et al., 1998). Here the quality-assured level 2.0 data are used. For the comparison with the MODIS/Aqua composite AODs, the AERONET AOD values at 550 nm are obtained by interpolating the values at 440 nm and 870 nm on a log-log plot assuming linearity between the two channels (Remer et al., 2005). Fig. 2.2 shows scatterplot comparison of the MODIS/Aqua composite AODs gridded on $2^{\circ} \times 2.5^{\circ}$ to AERONET AODs at 11 sites during the period of 2006 to 2010. Both observations show a moderate agreement between each other with the correlation coefficient of 0.79 and the regression slope of 1.06. The result is consistent with the previous study by Hsu et al. (2006) who showed that the Deep Blue AODs were generally within the range of AERONET AODs, with 20-30% errors.

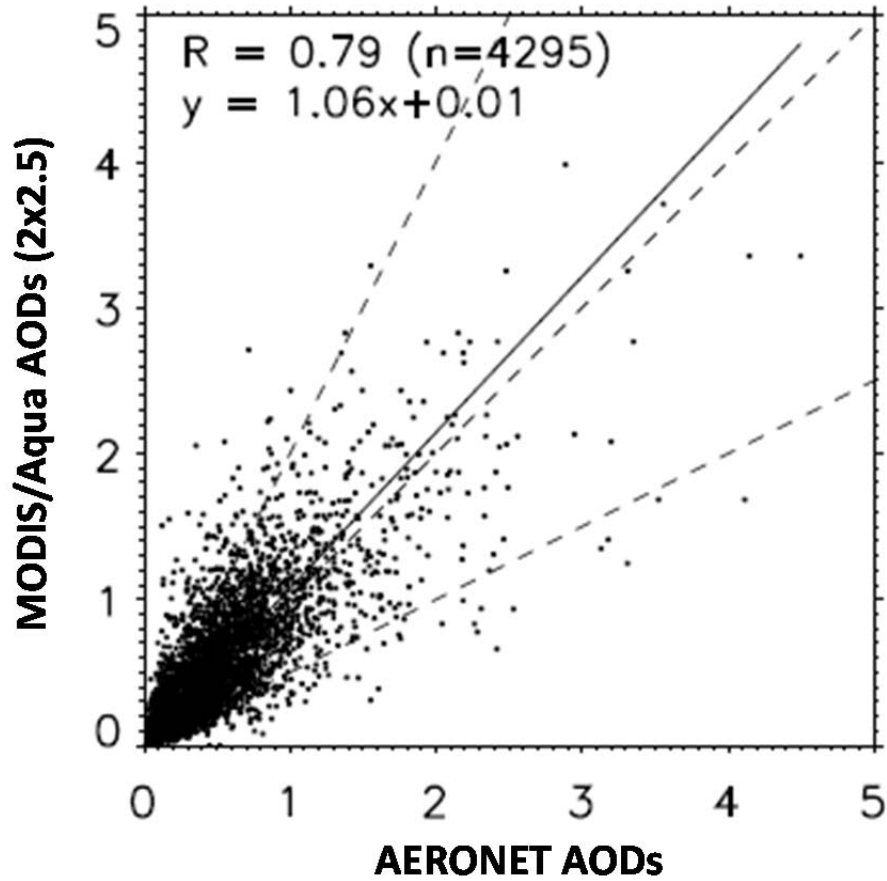


Figure 2.2. Scatterplots of AERONET versus MODIS/Aqua AODs. The 11 AERONET sites in East Asia are used during the period of 2006 to 2010 and the AERONET AODs are averaged around the overpass time of the AQUA platform over East Asia (1:30 PM). The horizontal resolution of MODIS AODs is regridded to $2^{\circ} \times 2.5^{\circ}$ for comparison to the model. The dashed lines indicate the 2:1, 1:1, and 1:2 lines.

2.3. Inverse model

2.3.1. Description

Inverse modeling is a formal approach for estimating the variables driving a system by taking measurements of the manifestations of that system, and using our physical understanding to relate these observations to the driving variables (Jacob, 2007). The variables to estimate are assembled into a state vector \mathbf{x} and the observations into an observation vector \mathbf{y} . The relationship between \mathbf{x} and \mathbf{y} is described by a physical model \mathbf{F} :

$$\mathbf{y} = \mathbf{F}(\mathbf{x}, \mathbf{b}) + \boldsymbol{\varepsilon} \quad (2.3)$$

where \mathbf{b} is a parameter vector including all model variables (parameters) and $\boldsymbol{\varepsilon}$ is an error including contributions from errors in the observations, in the forward model, and in the model parameters. From inversion of equation (2.3), \mathbf{x} is obtained to given \mathbf{y} . In the presence of error, the optimal solution of \mathbf{x} (called a posteriori) which reflects statistical estimates and weighs against a priori state vector \mathbf{x}_a , is obtained.

In this study, the inverse model defines the strength of the dust emissions from the individual source regions shown in Fig. 2.1 as a state vector that is optimized using observations based on the Bayesian least-squares method. Dust

aerosol concentrations are determined by emission, dry and wet deposition, and transport as described in the previous section. Changes in dust aerosol concentrations to these processes are all first-order dependent. In particular, dust aerosol concentrations vary linearly depending upon dust emissions. As shown in equation (2.4), the observation vector \mathbf{y} represents either the PM_{10} measurements in the surface air or the satellite AODs that can be related to the state vector \mathbf{x} of the dust aerosol emissions:

$$\mathbf{y} = \mathbf{K}\mathbf{x} + \boldsymbol{\varepsilon} \quad (2.4)$$

where \mathbf{K} is the Jacobian matrix that indicates the forward model described in the previous section. It does not depend on the state vector under linear assumption that is to relate the sources to the concentrations in a forward sense. The state vector includes not only dust emissions from the individual source regions but also a sum of non-dust aerosol emissions including sulfate, nitrate, ammonium, black carbon, organic carbon, and sea salt aerosols over East Asia because the PM_{10} mass concentrations and satellite AODs may include fractions of non-dust aerosols even during severe dust storm periods. The AODs in the model are calculated at 550 nm using the Mie algorithm (Wiscombe, 1980) and physical parameters including the effective dry diameters and the refractive indices for all aerosols such as dust, sulfate, nitrate, ammonium, black carbon, organic carbon, and sea salt aerosols (Chin et al., 2002). The error vector $\boldsymbol{\varepsilon}$ includes contributions

from the measurement accuracy, subgrid variability of the observations, and errors in the forward model. The characteristics of these errors are described by the observational error covariance (\mathbf{S}_ε) below.

The optimized dust source is defined as that which minimizes an error-least squares (chi-squared) scalar cost function $J(\mathbf{x})$, derived from Bayes' theorem with the assumption of Gaussian errors (Rodgers, 2000).

$$\mathbf{J}(\mathbf{x}) = (\mathbf{y} - \mathbf{K}\mathbf{x})^T \mathbf{S}_\varepsilon^{-1} (\mathbf{y} - \mathbf{K}\mathbf{x}) + (\mathbf{x} - \mathbf{x}_a)^T \mathbf{S}_a^{-1} (\mathbf{x} - \mathbf{x}_a) \quad (2.5)$$

where \mathbf{x}_a is the a priori state vector and \mathbf{S}_a is the error covariance matrix for the a priori state vector (\mathbf{x}_a). The superscript \mathbf{T} represents the transpose operator of a matrix. The first term on the right hand side of equation (2.5) means the mismatch between the simulations and the observations weighted by the observational error covariance. The second term represents the departure of the true value of the state vector from the a priori estimate, weighted by the error covariance of the a priori state vector.

The solution for minimization of a cost function with respect to \mathbf{x} is such that $\nabla_{\mathbf{x}} \mathbf{J}(\mathbf{x}) = 0$ defines the Maximum A Posteriori (MAP) solution of the inversion problem. The optimized a posteriori state vector ($\hat{\mathbf{x}}$) (Rodgers, 2000) is given as follows:

$$\hat{\mathbf{x}} = \mathbf{x}_a + (\mathbf{K}^T \mathbf{S}_\varepsilon^{-1} \mathbf{K} + \mathbf{S}_a^{-1})^{-1} \mathbf{K}^T \mathbf{S}_\varepsilon^{-1} (\mathbf{y} - \mathbf{K}\mathbf{x}_a) \quad (2.6)$$

The a posteriori error covariance matrix ($\hat{\mathbf{S}}$) is computed as follows:

$$\hat{\mathbf{S}} = (\mathbf{K}^T \mathbf{S}_e^{-1} \mathbf{K} + \mathbf{S}_a^{-1})^{-1} \quad (2.7)$$

Equations (2.6) and (2.7) are sequentially applied for the inverse analyses that are conducted separately using the daily PM₁₀ observations in the surface air and the satellite AODs.

2.3.2. Error specification

The error covariance (\mathbf{S}_a) of the a priori state vector (\mathbf{x}_a) is assigned an uncertainty of 200% for individual dust source estimates, based on recent global model estimates of dust emissions, which differ by more than a factor of two (Miller et al., 2004; Werner et al., 2002). For dust emissions from the rest of the world (RoW) and non-dust aerosol emissions, the error of the a priori state vector is arbitrarily assigned an uncertainty of 10% for each source. This value is relatively lower than the former uncertainty value because main focus of this study is the best estimation of dust sources over East Asia.

The observational error covariance (\mathbf{S}_e) can be decomposed into a sum of error covariance matrices describing the instrument error, the representation error, and the forward model error.

For the inverse model with the ground-based PM₁₀ concentrations, the forward model errors during periods 1 and 2 are assumed to be 93% and 200% respectively that are estimated from the relative residual standard deviation (RRSD) of the difference between the PM₁₀ observations and the colocated model PM₁₀ concentrations with a priori sources during periods, as represented by $(\mathbf{K}\mathbf{x}_a - \mathbf{y})/\mathbf{y}$ (Palmer et al., 2003). It is assumed that the mean bias is due to errors in the a priori sources and that the variance about this mean value represents uncertainty due to the model. The representation errors during periods 1 and 2 are 83% and 65% respectively, which are calculated by the standard deviation of the observed PM₁₀ concentration from its mean value. The instrumental error of the PM₁₀ mass concentrations is assigned an uncertainty of 10%. The sensitivity of the a posteriori solution to the associated error estimations and the data selection are assessed in section 4.2.

For the inverse model analysis with the MODIS AODs, the forward model error is assigned for the individual 2°×2.5° model grids. It is estimated from the RRSD of the difference between the observed and the modeled AODs in each grid. The resulting model errors during period 2 are shown in Fig 2.3.

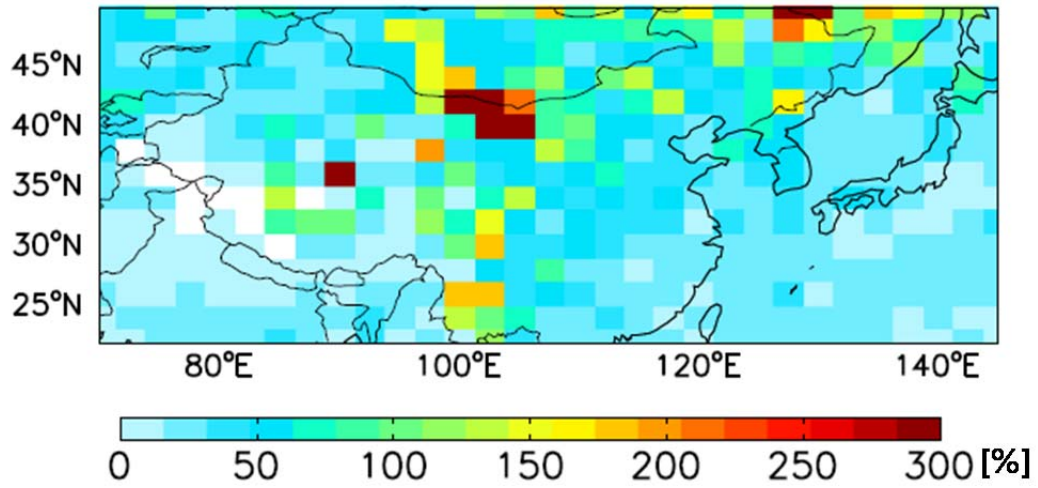


Figure 2.3. Model error variance for the MODIS AOD data in May 2007 using GEOS-Chem as a forward model during 00-07 UTC for the satellite overpass time in East Asia. White areas indicate missing data.

Values are largest over the Gobi Desert and also large in Mongolia and South China but relatively small in the Taklamakan Desert. This spatial difference of the model errors is attributed to the source function in the model that determines a spatial distribution of dust sources based on the relative depression of surface topography (Ginoux et al., 2001). The Gobi Desert and Mongolia including other dust source regions are susceptible to temporal surface type changes such as vegetation cover but the Taklamakan Desert is within a large desert basin that is bare soil surface all the year. Therefore, using the constant source function for the Taklamakan Desert appears to be relatively successful to simulate dust emissions than other dust source regions. The source function is discussed to improve model dust emission estimates in section 5.3.

The representation error during period 2 is estimated by the variability of MODIS Deep Blue AOD data ($1^\circ \times 1^\circ$ resolution) over the model grid ($2^\circ \times 2.5^\circ$ resolution) that is typically about 47%. The measurement error of MODIS Deep Blue AOD is assigned 20% that is a bias resulted from comparing with the AERONET AOD observed at available 5 sites (SACOL, Beijing, Xianghe, Issyk-Kul, Kanpur) among the 11 stations as shown in Fig. 2.1.

Overall, critical difference for the specification of observational errors with both observation data is that the forward model errors with the ground-based

PM₁₀ concentration are uniform everywhere whereas those with the MODIS Deep Blue AODs differ in each model grid.

CHAPTER III

Model evaluation with a priori dust sources

3.1. Simulation of dust events in April 2001 (period 1)

In spring 2001, intense Asian dust storms occurred on several occasions (Darmenova et al., 2005; Gong et al., 2003). Among these, a particularly strong dust storm occurred over the Taklamakan Desert and deserts in China and Mongolia on 6 April 2001 (Liu et al., 2003). This dust storm moved eastward to Northeastern China, resulting in widespread poor visibility in Northern China. The dust reached the Korean peninsula on 8 April and Japan on 9 April (Gong et al., 2003; Liu et al., 2003). This East Asian dust storm was the most severe event on record and significantly affected surface PM concentrations as far as the United States (Jaffe et al., 2003; Zhao et al., 2008). The other major dust storm in April 2001 began in the Taklamakan and Gobi deserts on 29 April (Gong et al., 2003). In this case, dust aerosols were transported directly eastward by strong meridional flow promoted by a deep trough formed west of Japan. This dust storm affected downwind regions such as Korea and Japan and the west coast of North America to a lesser extent (Gong et al., 2003).

This study focuses on these well-documented dust events to evaluate the model output. Figs. 3.1-3 show comparisons between the observed and simulated PM₁₀ mass concentrations with a priori sources at sites in China, Korea, and Japan. The high modeled PM₁₀ concentrations are mainly the result of dust aerosols from the southern region of the Gobi Desert (S5; blue colored) and deserts in Northeastern China (S8; orange colored) and Mongolia (S2; red colored). During the dust events, the modeled concentrations are generally higher than the observations near the source regions of China. Dust aerosol from the southern Gobi Desert is a major contributor to the high PM₁₀ concentrations in the model. From the end of April to the beginning of May, the model shows remarkably higher PM₁₀ concentrations compared to the observations over China, particularly at Huhehaote and Zhenzhou that are located close to the dust source regions. These elevated PM₁₀ concentrations in the model mainly result from the high contribution from the southern region of the Gobi Desert.

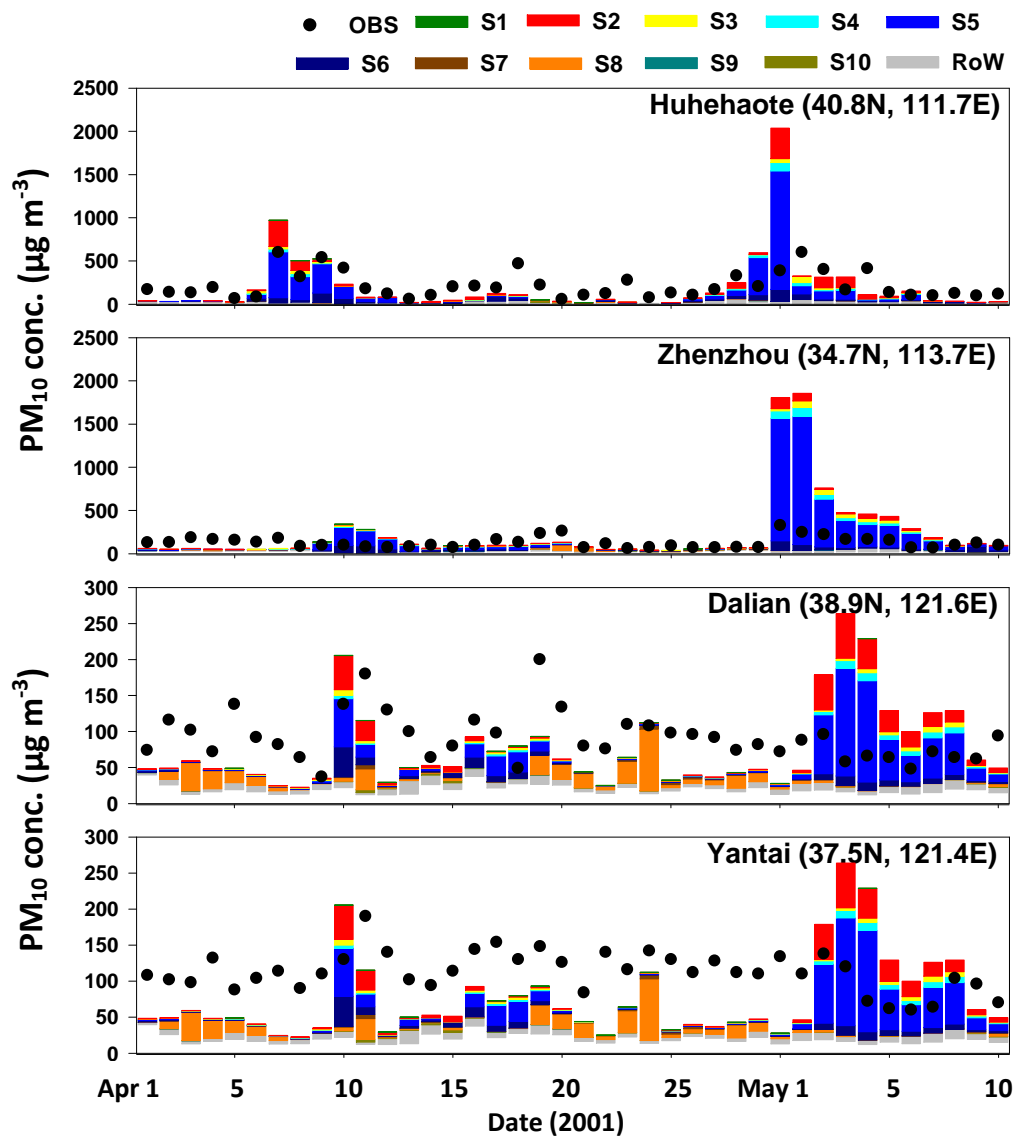


Figure 3.1. Observed daily PM₁₀ concentrations versus modeled PM₁₀ concentrations with the a priori emissions at Huhehaote, Zhenzhou, Dalian, and Yantai in China from 1 April to 10 May in 2001. Black dots show observations and colored bars show simulated concentrations. Different colors indicate the individual contributions of dust aerosols from each source region; non-dust aerosols are shown in white.

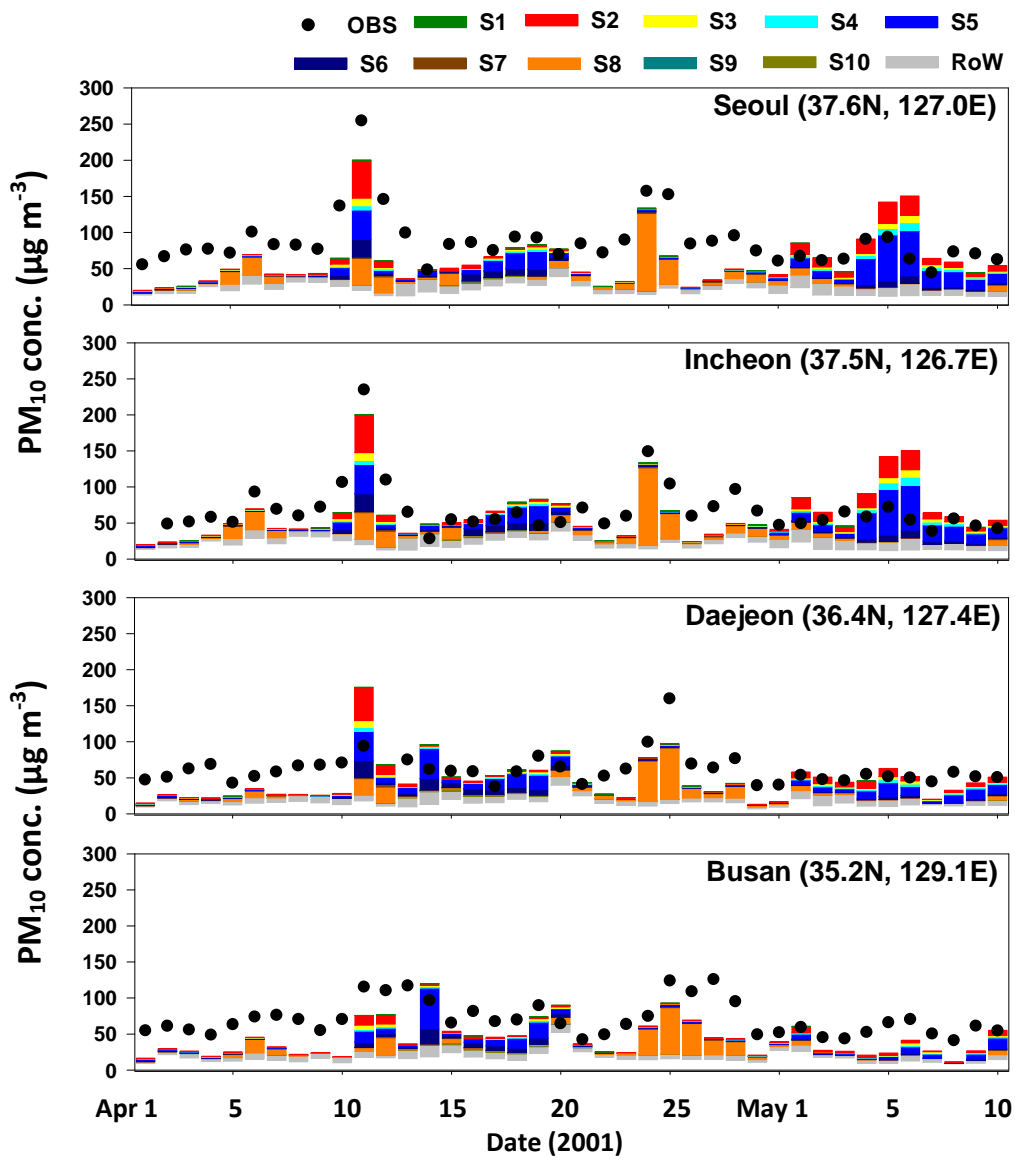


Figure 3.2. Same as in Fig. 3.1 but at Seoul, Incheon, Daejeon, and Busan in Korea.

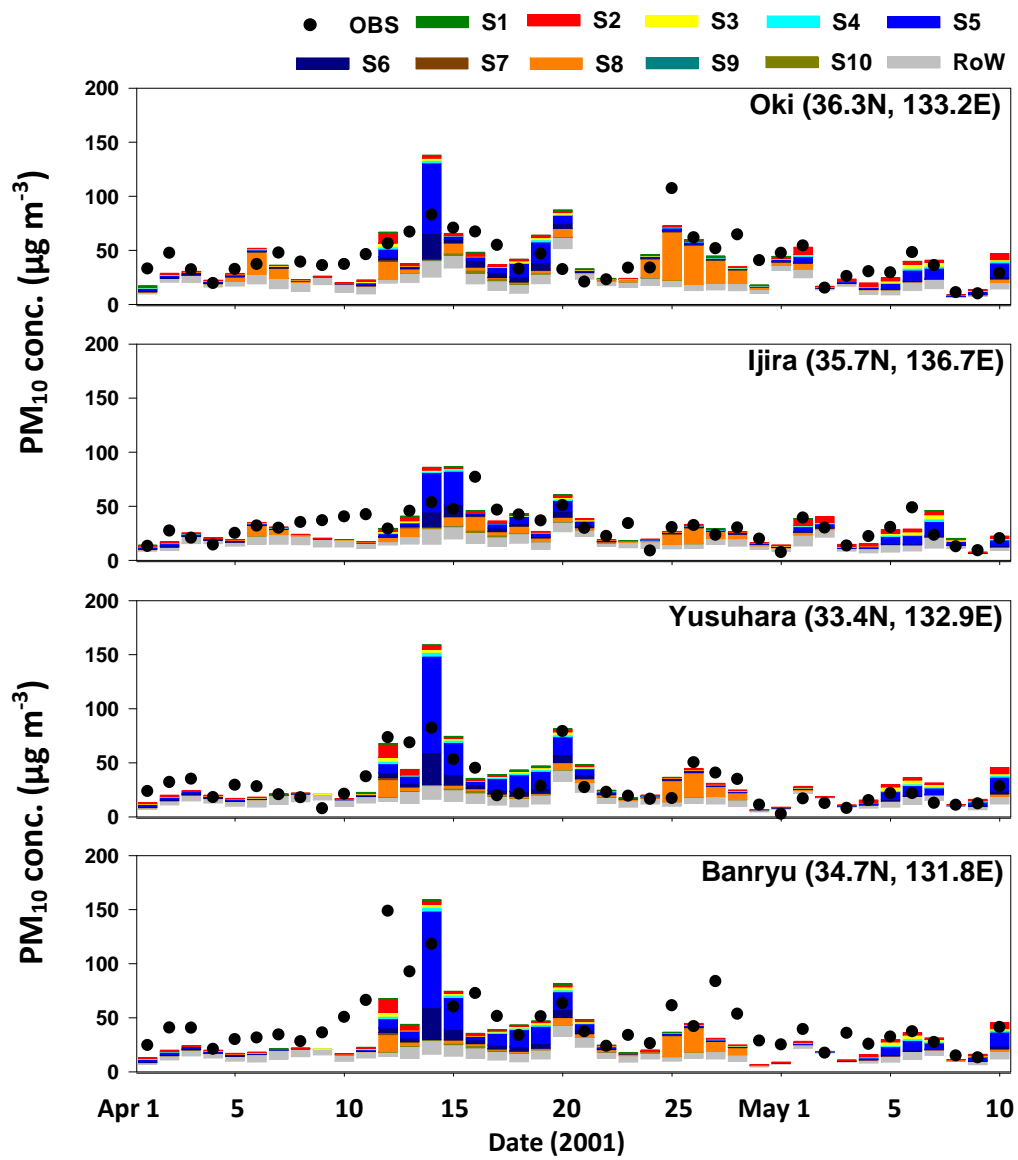


Figure 3.3. Same as in Fig. 3.1 but at Oki, Ijira, Yusuhara, and Banryu in Japan.

Korea and Japan were also affected by the two dust outbreaks in April. The first event affected Korea from 9–14 April, and hourly averaged PM_{10} concentrations in Seoul exceeded $800 \mu\text{g m}^{-3}$ on 11 April. This dust primarily originated from the Gobi Desert and affected the middle of the Korean peninsula and Southwestern Japan most significantly. Busan, in Southern Korea, appeared less affected by this dust outbreak than Seoul and Incheon which are located relatively north. The model reproduces the observed PM_{10} concentrations in Korea relatively well. However, at sites in Japan, the simulated PM_{10} concentrations exceed observed concentrations during this period because of the high dust aerosol concentrations from the Gobi Desert in the model. Dissimilar transport pathways of the dust aerosols result in different source contributions to the PM_{10} concentrations in downwind regions. The second dust event from 24–26 April reached a peak PM_{10} concentration of $920 \mu\text{g m}^{-3}$ in Korea on 24 April. This dust was primarily from Inner Mongolia and Manchuria, which are located closer than other source regions to Korea. The dust aerosols from these sources more directly affected Korea.

In contrast, model values are generally lower than observations during non-dust storm periods, even at sites close to the source regions. This low bias is attributed to a lack of fugitive dust emissions in the model. Fugitive dust from unpaved roads, agricultural soil, construction, and disturbed surfaces in local

regions substantially contributes to the fraction of PM_{10} mass concentrations. Huang et al. (2010b) reported that the main local contributions of PM_{10} in Beijing were stationary emissions, road dust emissions, construction site dust emissions, and fugitive industrial emissions that accounted for 60% of the total emission sources. Moreover, Jang et al. (2008) estimated that fugitive dust emissions accounted for three quarters of the total PM_{10} emissions in the capital region of Korea.

3.2. Simulation of dust events in May 2007 (period 2)

Intense dust storms occurred from the Gobi and Sand Deserts and swept across vast areas of East Asia during 21–31 May 2007. Dust aerosol mobilization and transport were manifested by a large-scale low pressure system initiated in Northern Mongolia that provided favorable synoptic conditions for mobilization and transport of dust aerosols from the source to the downwind regions (Hara et al., 2009). Fig. 3.4 shows the modeled daily mean column concentrations of dust aerosols with a priori sources and SYNOP reports containing weather codes associated with dust phenomena from 21 to 28 May 2007. Dust occurrences including blowing sand and dust storm are denoted with red colored symbol S, and floating dust is indicated with blue colored symbol S. On 23 May, the strong surface winds over Southern Mongolia initiated dust storms that were transported to the east of Mongolia and Northeastern China on 24 May and arrived in Korea on 25 May. At the same time, another low-pressure system was developed in the northern part of Mongolia and associated strong winds on the southern side of the low-pressure system caused second dust storm that was rapidly moved to Korea and Southern Japan where both dust storms were eventually merged. The SYNOP observations near the downwind region as well as source region indicated the occurrence of dust storms and floating dust and are

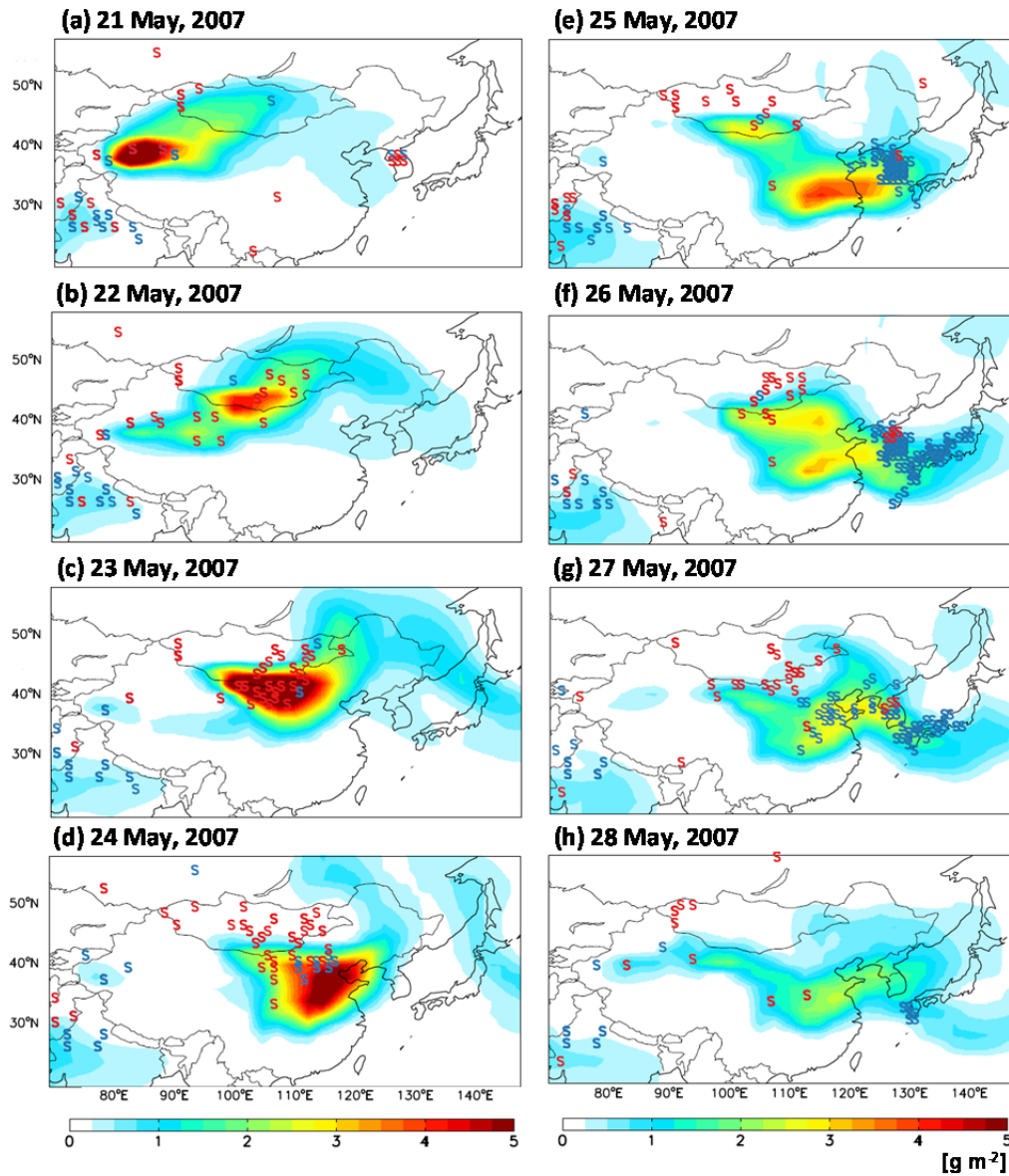


Figure 3.4. Modeled column concentrations of dust aerosols with a priori sources and SYNOP dust code (S) from 21 to 28 May in 2007. The red colored S represents blowing sand (code #7, 8) and dust storm (code #9, 30, 31, 32, 33, 34, 35, 98) and the blue colored S indicates floating dust (code #6).

in good agreement with the spatial distribution of modeled dust aerosol column concentrations.

Fig. 3.5 shows a comparison of daily mean modeled AODs with composite MODIS AODs from 21 to 28 May 2007. The model AODs are calculated during 00-07 UTC for the satellite overpass time in East Asia. As shown in Fig. 3.5, both MODIS AODs and modeled AODs present high values in Northeastern China but the model is generally lower than MODIS in Eastern China as shown in previous studies (Choi et al., 2009; Jeong et al., 2008). On the other hand, MODIS AODs are missing over the dust source regions (indicated with white areas) during 21-23 May when the model simulates a large amount of dust emissions in the dust source regions such as the Taklamakan Desert, Mongolia and the Gobi Desert. Not only bright surfaces but also cloud covers associated with low pressure systems hinder MODIS AODs retrievals.

In addition, the model simulates high AODs due to forest fires over the eastern part of the border between Russia and China on 24 May. Whereas these high AODs are not shown in MODIS observations that misclassify high AOD values as cloud-contamination pixels such that any retrieved AODs greater than 5.0 are removed. This criterion is typically effective, yet during extreme events aerosol plumes may be mistaken for cloud (van Donkelaar et al., 2011). Therefore, a care must be taken to deal with MODIS AODs over the source

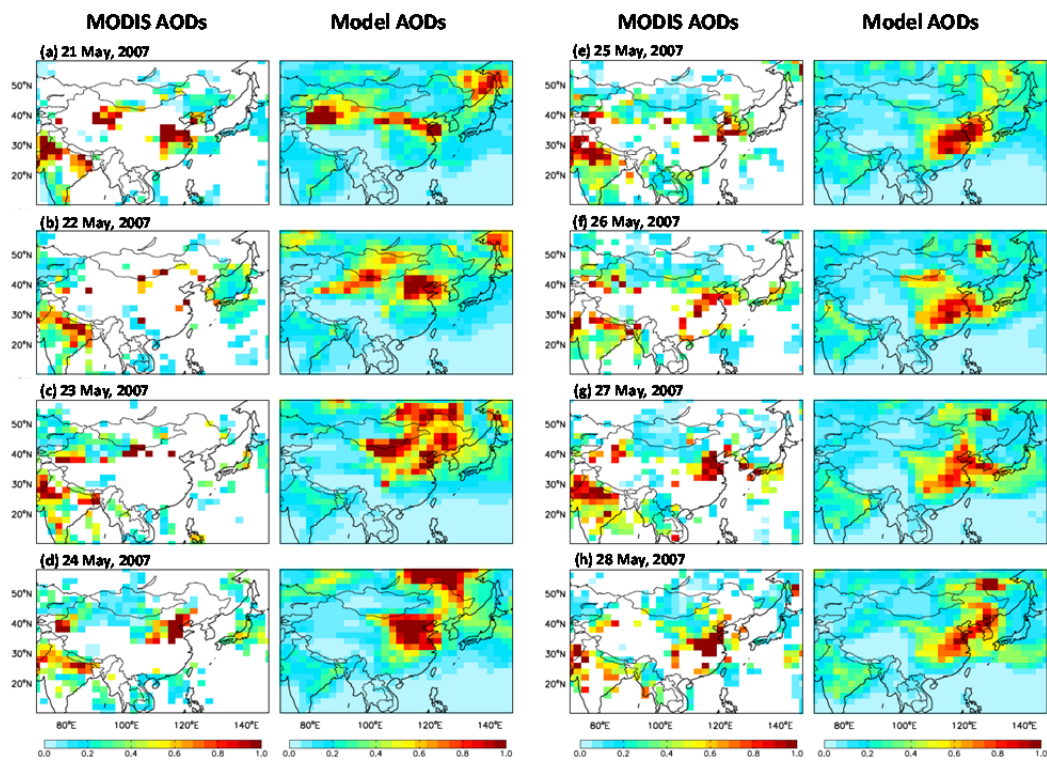


Figure 3.5. Daily MODIS AODs versus modeled AODs with a priori sources from 21 to 28 May in 2007. The horizontal resolution of MODIS data is regridded to $2^{\circ} \times 2.5^{\circ}$ and white areas indicate missing data.

regions where severe aerosol events might occur. While the modeled high AODs over the downwind regions including Northeastern China, Korea and Japan consistent with MODIS AODs during 25-28 May.

Simulated PM₁₀ mass concentrations in the surface air are compared against PM₁₀ observations in Fig. 3.6. During dust events, the modeled concentrations with a priori sources are much higher than the observations over downwind regions as well as source regions. Dust aerosols from Mongolia (S2; red colored) and the southern area of the Gobi Desert (S5; blue colored) are major contributors to the high PM₁₀ concentrations in the model. From 23 to 31 May, the model shows remarkably higher PM₁₀ concentrations compared to the observations, thereby the modeled concentrations are highly biased relative to the observations in China and Korea.

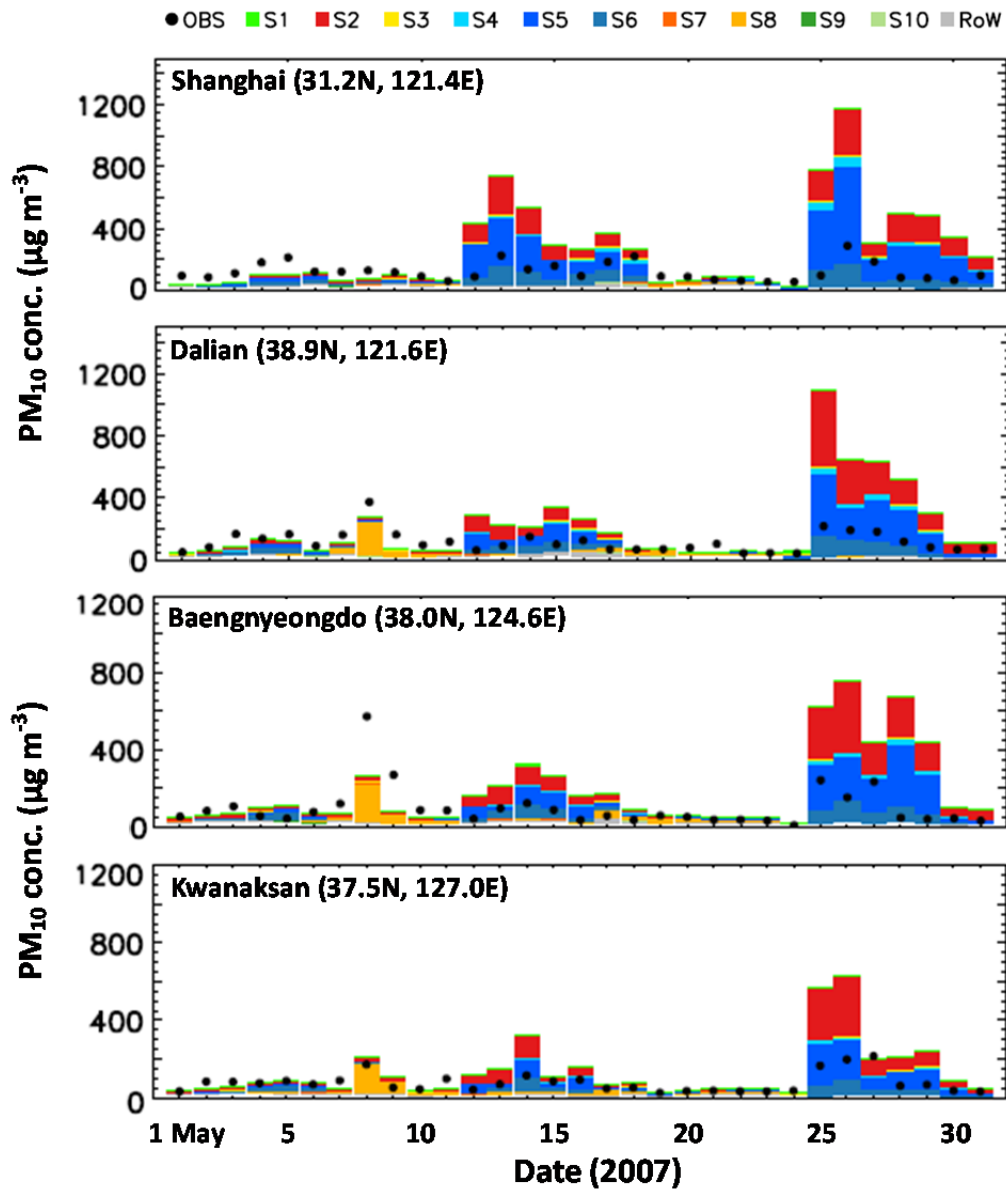


Figure 3.6. Observed daily PM₁₀ concentrations versus modeled PM₁₀ concentrations with the a priori emissions at Shanghai and Dalian in China, Baengnyeongdo and Kwanaksan in Korea for May 2007.

Fig. 3.7 presents scatterplots comparisons of the observed versus simulated daily mean PM_{10} concentrations in the surface air for May 2007. Correlation coefficients between the model and the observation are 0.46 in China, 0.58 in Korea, and 0.79 in Japan, showing improvements away from the source regions. This indicates that errors in the model are largely due to dust emissions over the source regions and get reduced toward the downwind regions where the transport in the model largely determines spatial and temporal distributions of dust aerosols. However, the model shows significant high bias as indicated with regression slopes of 5.7, 4.2, and 4.1 for China, Korea, and Japan, respectively. Overestimated dust concentrations from the Gobi Desert and Mongolia are likely reason for this bias.

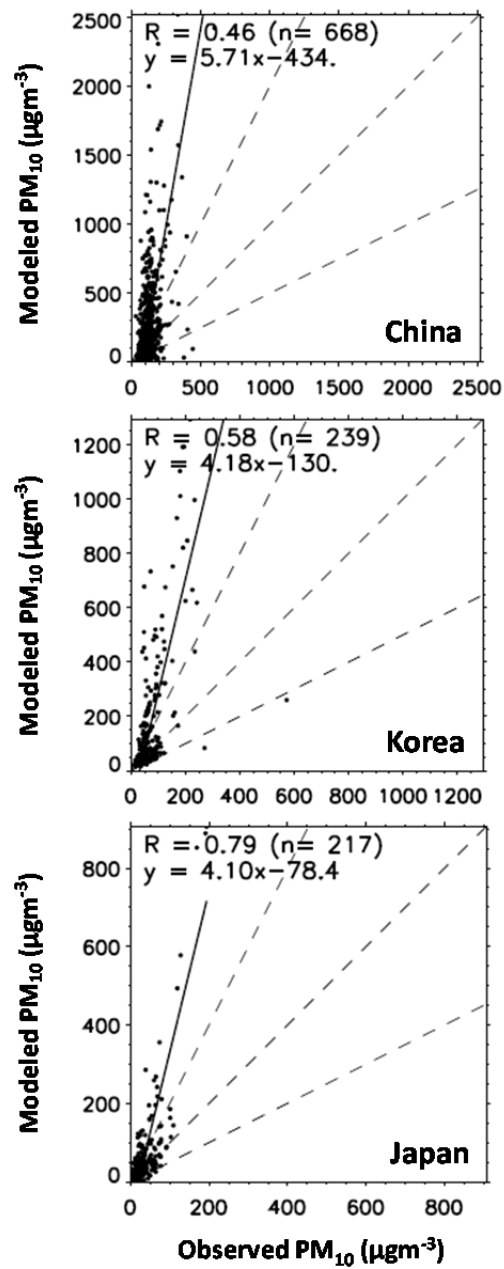


Figure 3.7. Scatterplots of the observed versus simulated PM₁₀ mass concentrations with a priori dust sources at China, Korea, and Japan in May 2007.

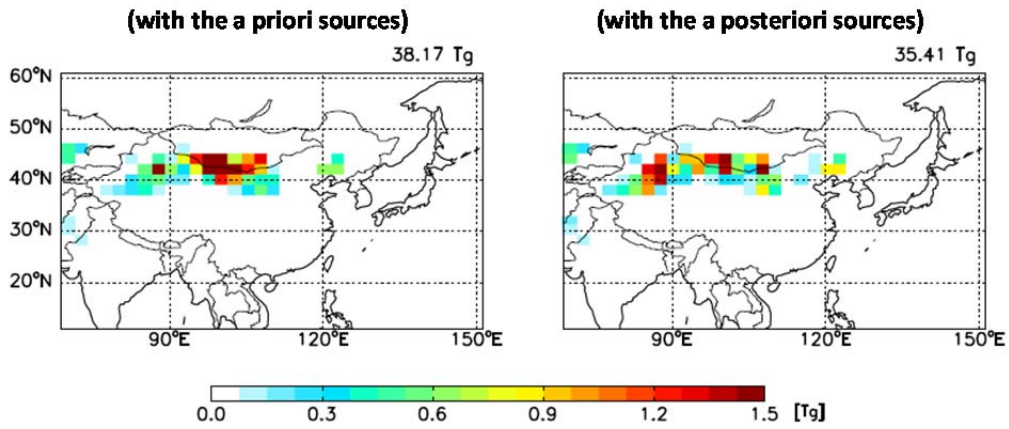
CHAPTER IV

Inverse modeling analysis of dust sources during the period 1

4.1. A posteriori dust sources from PM₁₀ observations

Here, the optimized dust sources over East Asia from inverse modeling analysis are presented and evaluated with the observations. The a priori dust sources discussed in section 3.1, yield 38.2 Tg over Asia (10–60°N, 70–150°E) in April 2001. The dominant source region is the southern area of the Gobi Desert (S5), contributing ~40% of the total dust emission, followed by Mongolia (S2) and the Taklamakan Desert (S3), which account for 21% and 14%, respectively. Fig. 4.1 shows the modeled dust emissions and concentrations with the a priori and a posteriori sources over East Asia. The simulated total dust emission with the a posteriori source is 35.4 Tg, slightly lower than the a priori value. Although there is only a slight change in the magnitude of total emissions between the a priori and a posteriori results, the spatial distribution of dust emissions is significantly altered.

Dust emissions



Dust concentrations in the surface air

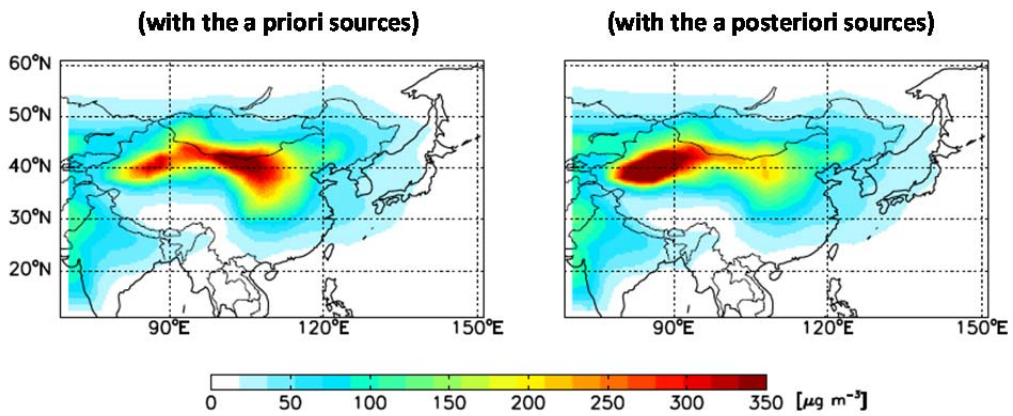


Figure 4.1. Simulated dust emissions (upper) and surface air dust concentrations (lower) of the a priori (left) and a posteriori dust sources (right).

Regions in which dust emissions changed significantly with the a posteriori sources are the southern regions of the Gobi Desert (S5), the Taklamakan Desert (S3), Eastern Mongolia and Inner Mongolia (S7), and Manchuria (S8). Over the Gobi Desert in China (S5), the a posteriori emission decreases by 76% relative to the a priori emission. Over the Taklamakan Desert (S3) and Eastern and Inner Mongolia (S7), the a posteriori sources increase two to three fold compared to the a priori sources. The a posteriori source in Manchuria (S8) also increases by 36% compared to the a priori source. The Manchuria source region is close to the Korean peninsula and the resulting change improved the simulations in Korea. The a posteriori sources over historical deposition areas (S9 and S10) increase by 26% and a factor of 3, respectively. However, the effects of these changes on PM₁₀ concentrations are trivial, as these areas are minor source regions accounting for less than 1% of the dust emissions over East Asia. Changes in the individual source regions are summarized in Table 4.1.

Table 4.1. Inverse modeling analysis of dust sources over East Asia in the domain 10–60°N, 70–150°E for April 2001.

A priori sources (Tg mon ⁻¹)												
Regions	S1	S2	S3	S4	S5	S6	S7	S8	S9	S10	RoW	Total
Emissions	0.33	8.03	5.51	3.14	15.39	2.60	0.11	1.63	0.02	0.07	1.34	38.17
(%)	(0.9)	(21.0)	(14.4)	(8.2)	(40.3)	(6.8)	(0.3)	(4.3)	(0.1)	(0.2)	(3.5)	(100)
A posteriori sources (Tg mon ⁻¹)												
Regions	S1	S2	S3	S4	S5	S6	S7	S8	S9	S10	RoW	Total
Emissions	0.35	6.30	12.94	3.92	3.69	4.00	0.34	2.21	0.03	0.18	1.44	35.42
(%)	(1.0)	(17.8)	(36.5)	(11.1)	(10.4)	(11.3)	(1.0)	(6.2)	(0.1)	(0.5)	(4.1)	(100)
Ratios (a posteriori/a priori)												
Regions	S1	S2	S3	S4	S5	S6	S7	S8	S9	S10	RoW	
Ratios	1.1	0.8	2.3	1.2	0.2	1.5	3.0	1.4	1.3	2.6	1.1	

Figs. 4.2–4 also compare the observed versus simulated PM_{10} concentrations using the a posteriori sources in China, Korea, and Japan. The large bias with the a priori sources during the dust events (7–14 April, 29 April–5 May) is significantly reduced and the model shows better agreement with the observations. During 1 April to 10 May, the mean bias decreases from 82% to 65% in China. For downwind regions, the mean bias decreases from 41% to 38% in Korea and from 52% to 49% in Japan. This improvement is largely due to decreased dust emissions from the southern Gobi Desert and increased emissions from Northeastern China.

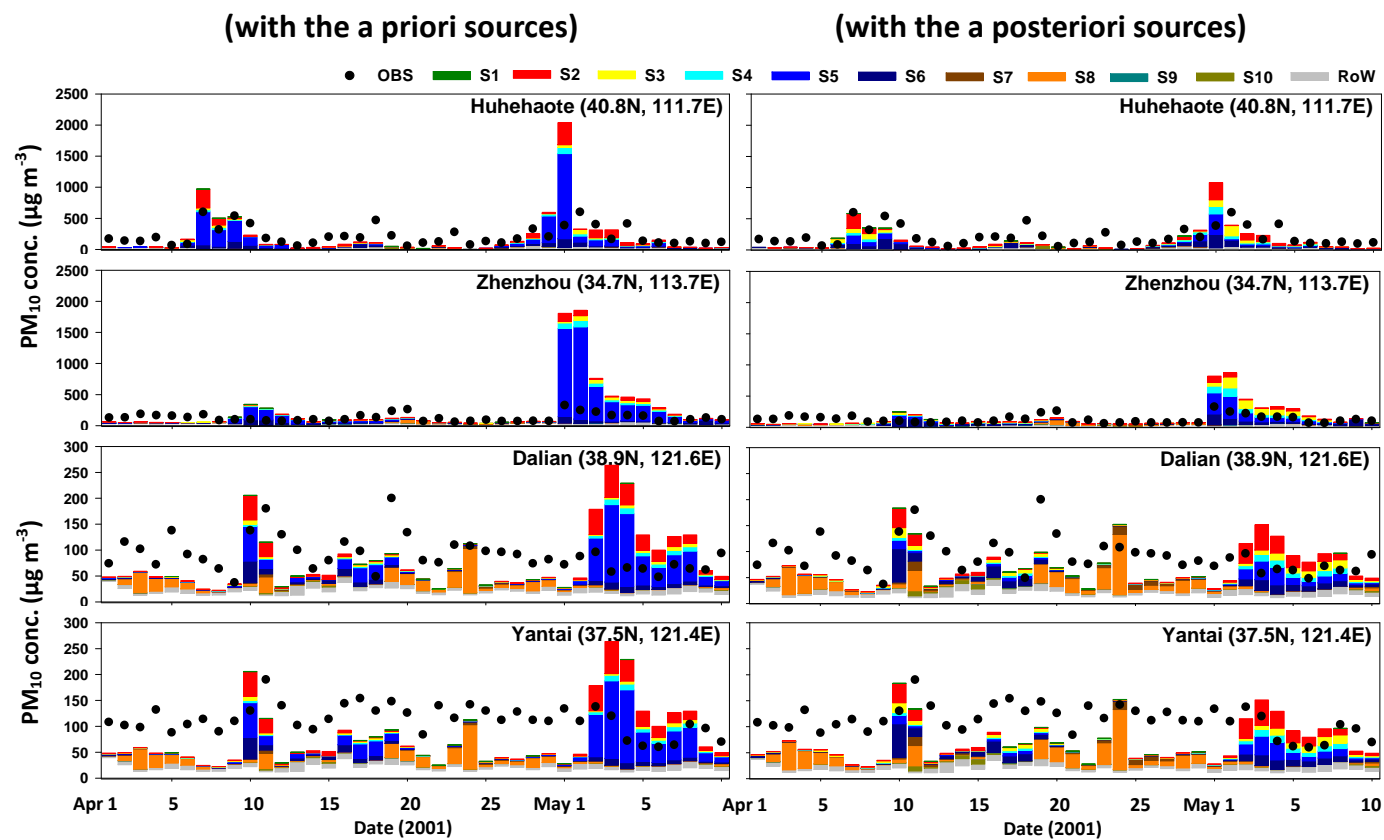


Figure 4.2. Observed daily PM₁₀ concentrations versus modeled PM₁₀ concentrations with the a priori emissions (left) and the a posteriori emissions (right) at Huhehaote, Zhenzhou, Dalian, and Yantai in China.

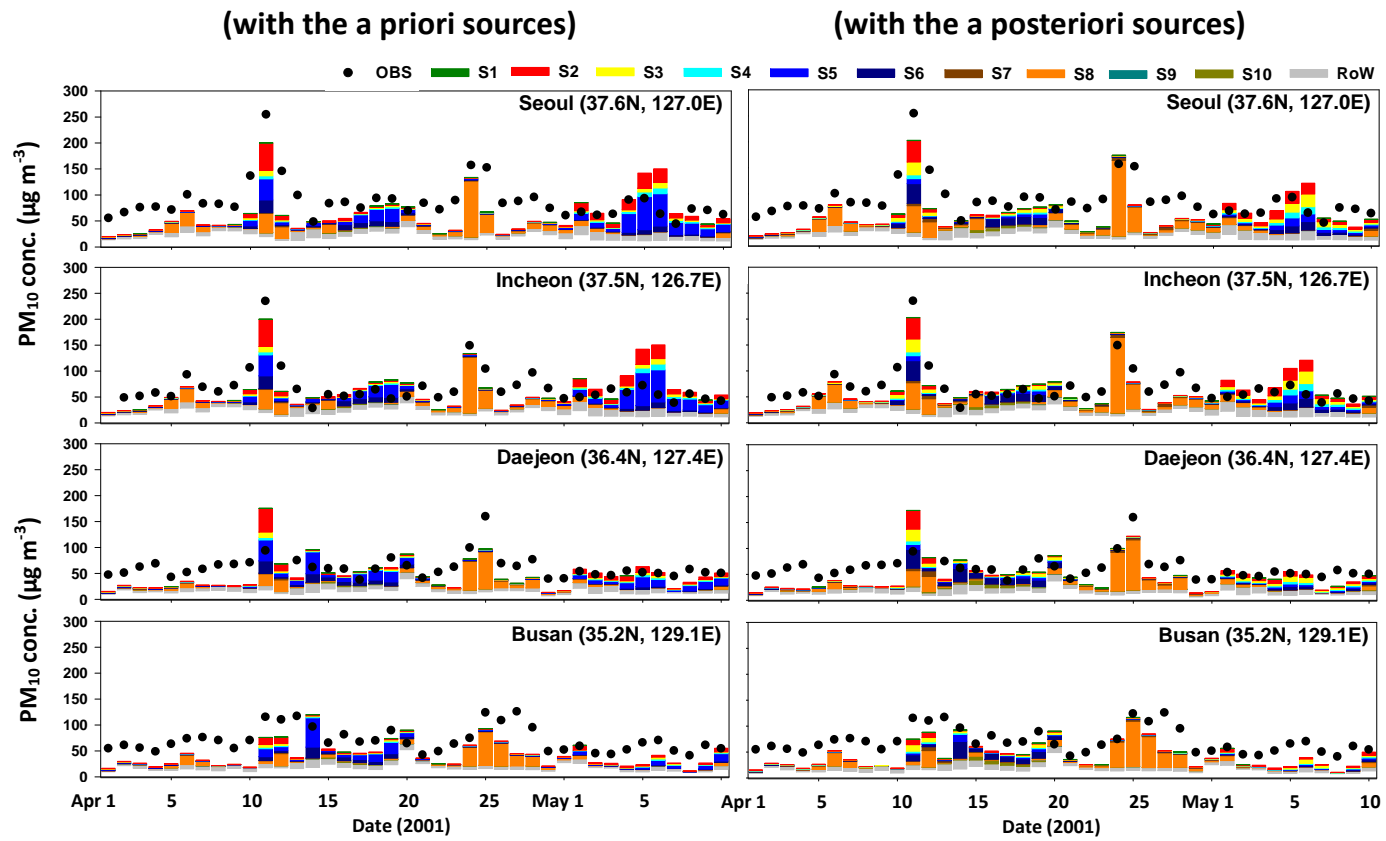


Figure 4.3. Same as in Fig. 4.2 but at Seoul, Incheon, Daejeon, and Busan in Korea.

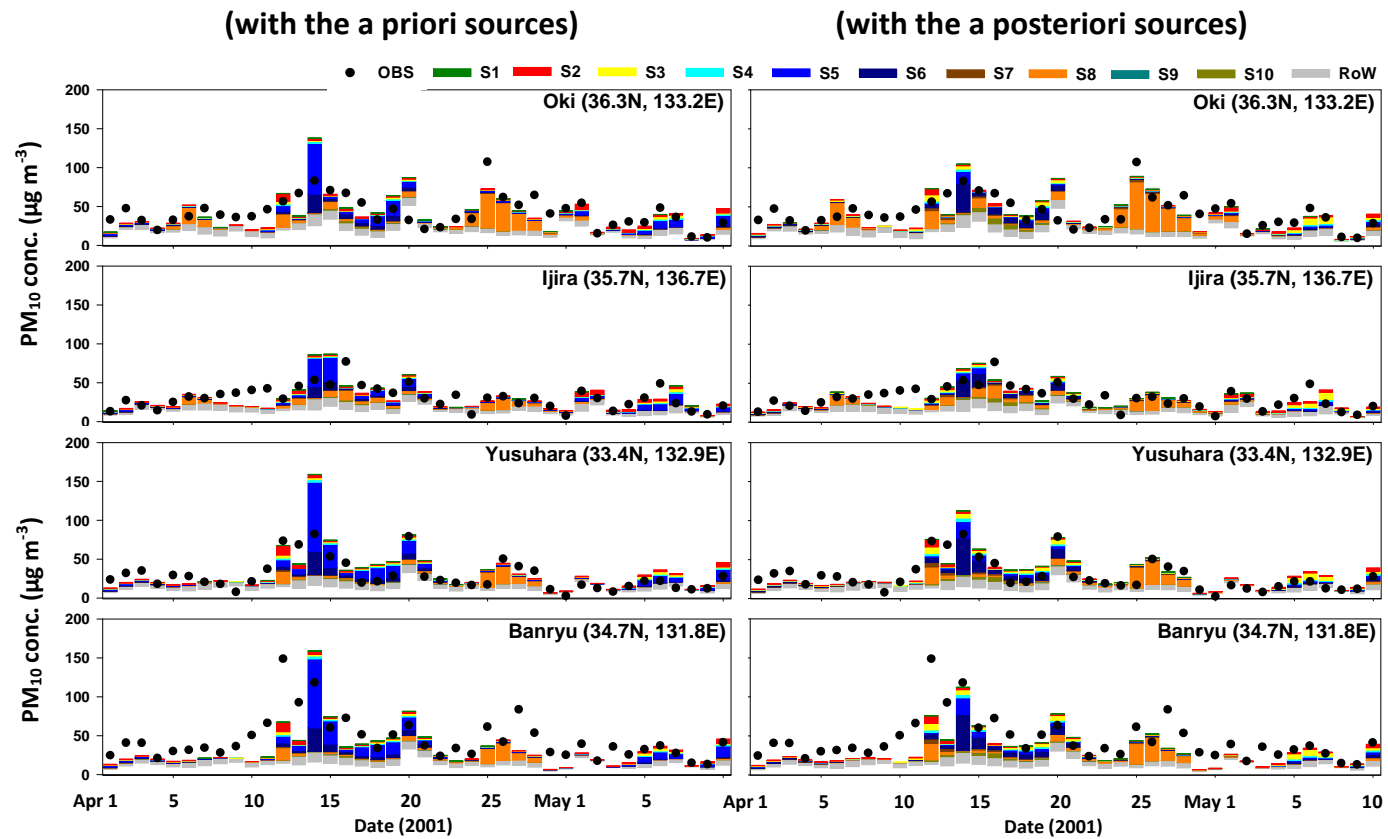


Figure 4.4. Same as in Fig. 4.2 but at Oki, Ijira, Yusuvara, and Banryu in Japan.

To evaluate the optimized dust sources independently, the aerosol index (AI) data of the Earth Probe Total Ozone Mapping Spectrometer (TOMS) and the AOD data from the Multi-angle Imaging Spectrometer (MISR) on-board the Earth Observing System (EOS) Terra satellite are used. TOMS AI is an excellent indicator of the presence of UV-absorbing aerosols, such as mineral dust and black carbon (Herman et al., 1997; Torres et al., 1998). Although TOMS AI is more sensitive to UV-absorbing aerosols at altitudes above 2 km and is distorted by the presence of clouds, it detects considerable dust activity (Prospero et al., 2002). MISR/Terra (Diner et al., 2001) provides near-global coverage of the AOD data in four narrow spectral bands centered at 446, 558, 672, and 866 nm. MISR can retrieve aerosol properties over a variety of terrains, including reflective surfaces such as deserts (Martonchik et al., 2004).

The spatial distribution of the monthly mean TOMS AI is compared with that of simulated column concentrations for dust and black carbon aerosols in April 2001 as shown in Fig. 4.5. The model results are sampled at 00-07 UTC for the satellite overpass time when the observations are available in East Asia. Horizontal resolutions of TOMS AI and model simulations are $1.0^{\circ} \times 1.25^{\circ}$ and $2.0^{\circ} \times 2.5^{\circ}$, respectively. The highest TOMS AI values are found in the Taklamakan Desert; values are also generally large in the Gobi Desert. The high values likely reflect the presence of absorbing dust aerosols because no apparent

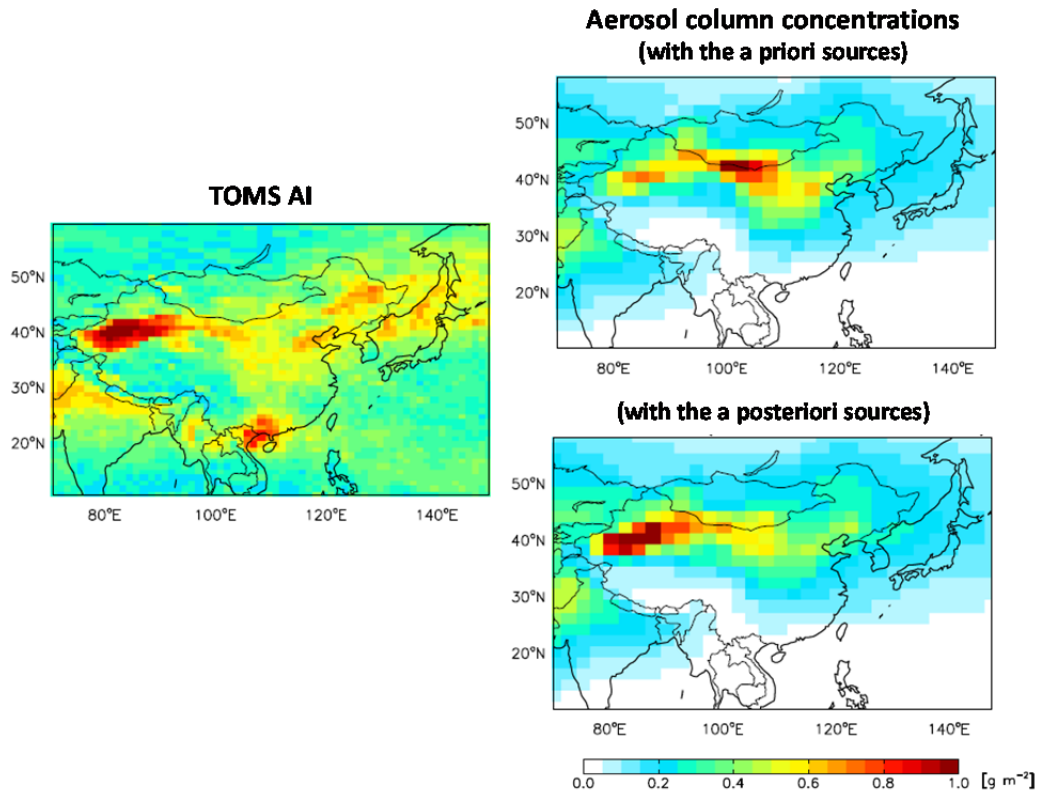


Figure 4.5. Aerosol Index (AI) from Total Ozone Mapping Spectrometry (TOMS) versus modeled column concentrations of black carbon and dust aerosols with the a priori and a posteriori dust sources in April 2001. The horizontal resolutions of TOMS AI and model simulations are $1.0^{\circ} \times 1.25^{\circ}$ and $2.0^{\circ} \times 2.5^{\circ}$, respectively.

sources of black carbon aerosols are present in these arid areas. The simulated dust column concentrations with the a posteriori sources reproduce the spatial distributions of TOMS AI very well, relative to the a priori sources.

The simulated AOD is also compared with the observed monthly mean AOD data from satellite measurements. Fig. 4.6 shows the AOD from MISR observations and the simulated values with the a priori and a posteriori sources in April 2001. The horizontal resolution of MISR data is $0.5^\circ \times 0.5^\circ$ and white areas indicate missing data. Scales of color bars are different for observations and simulations. MISR AOD is high in the Taklamakan Desert, Eastern China, and the northwestern Pacific Ocean. The simulated AOD with the a posteriori sources shows a similar spatial pattern and much better agreement with the observation relative to the a priori simulation.

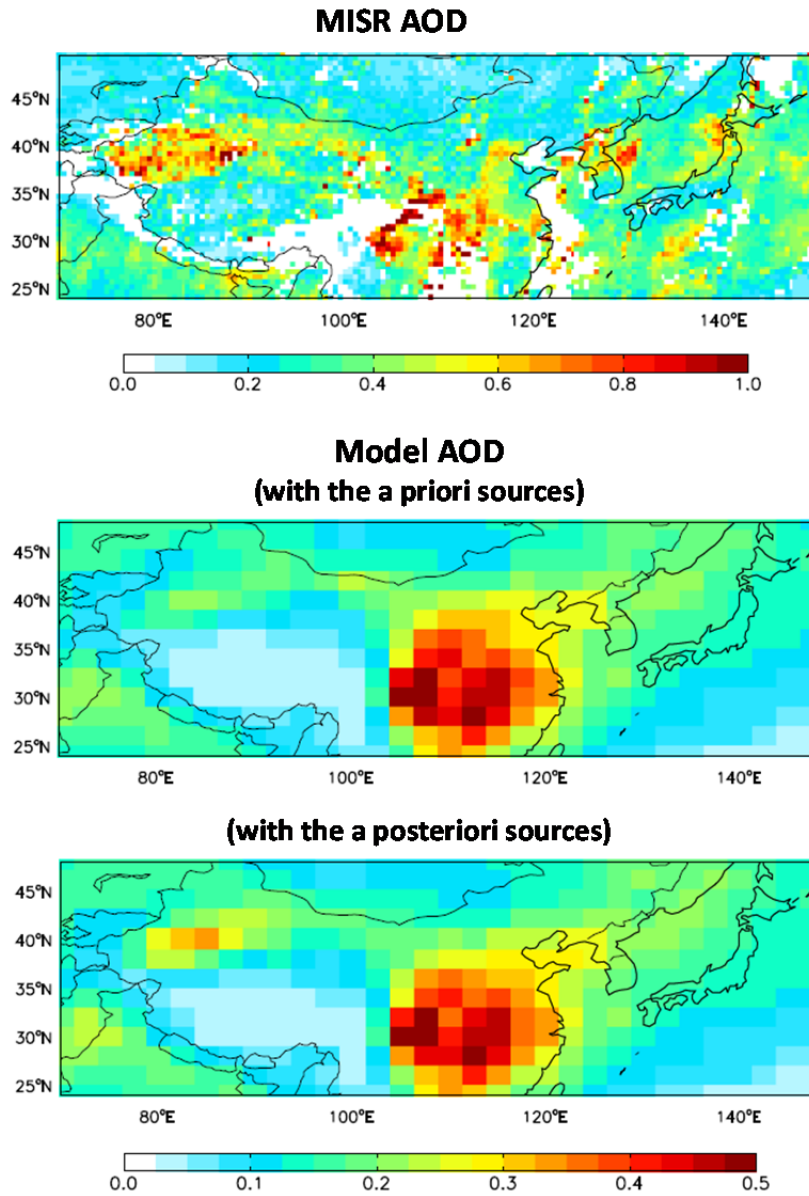


Figure 4.6. Monthly mean AODs from the Multi-angle Imaging Spectrometer (MISR) versus model values from the a priori and a posteriori sources in April 2001. The horizontal resolution of MISR data is $0.5^\circ \times 0.5^\circ$ and white areas indicate missing data. Note the difference in color scales.

The use of a posteriori sources enables us to better quantify the spatial and temporal distributions of dust aerosol concentrations and their contributions to air quality over East Asia. The inverse modeling analysis also identifies weaknesses in dust models reported in previous studies. For example, Tanaka and Chiba (2006) demonstrated that a model with coarse spatial resolution underestimated the dust emissions from the Taklamakan Desert because of insufficient representation of local wind. One of the challenges in dust modeling is to realistically represent subgrid-scale wind erosion processes at coarse model resolutions typically of more than 100 km. Lim and Chun (2006) reported that blowing sand events were becoming more frequent in Inner Mongolia as Asian dust source regions extended eastward from the Gobi, Tengger, and Ordos deserts to Inner Mongolia and Northeastern China, driven by eastward expanding desertification. In addition, Eastern Mongolia, Inner Mongolia, and Manchuria (China) have been suggested as major areas of desertification in recent decades (Chin et al., 2003). These observations are remarkably consistent with the changes in the inverse modeling results from a priori to a posteriori sources.

4.2. Issues with the inverse modeling analysis of dust emissions

The resulting inverse modeling analysis indicates that dust emissions in the southern regions of the Gobi Desert should substantially decrease, while increases are expected over the Taklamakan Desert and Northeastern China. However, the obtained results have some limitations. First, the strength and frequency of dust outbreaks display strong inter-annual variability, meaning that the best estimates of dust sources based on a single year observation may have considerable uncertainties. To overcome this issue, the physical processes responsible for dust source changes and the variations in these processes must be clarified by analysis of long-term observations.

In this analysis, observed PM_{10} concentrations are used to obtain the optimized dust sources because no direct dust observations are available over East Asia. These PM_{10} concentrations may not completely represent the dust aerosol concentrations. In addition, the PM_{10} concentrations in China retrieved from the API data have a cap of $600 \mu\text{g m}^{-3}$ that comprises about 2% of the data. These capped measurements may cause a low bias for tremendously strong dust storms. The use of direct dust observations both in the surface air and aloft would allow for better quantification of dust emissions and the 3-D distribution of dust aerosol concentrations over Asia.

Furthermore, uncertainty values are assumed to be 200% for the individual dust sources over East Asia, 10% for the rest of global dust sources and non-dust aerosol emissions, and also 10% for the instrumental error of the PM₁₀ mass concentrations. These uncertainties are arbitrarily assigned. To examine the sensitivity of the a posteriori sources to the assumed uncertainty values, several analyses are performed using different data sets and errors.

Fig. 4.7 shows a comparison between the a priori dust sources and the a posteriori dust sources from sensitivity analyses. Cases 1-2 are results from the same condition described above, except for 1% and 50% instrumental errors, respectively. These results are consistent with the previous a posteriori sources. Cases 3-4 have 150% and 250% errors, respectively, for dust sources using all the PM₁₀ observations from China, Korea, and Japan. Case 5 is the result from assigning different transport errors of 100%, 30%, and 70% for China, Korea, and Japan that are estimated by calculating the difference between the observations and models in each country. Cases 6-8 have 200% dust sources error and 93% transport error for different data selections. The data for case 6 include the PM₁₀ observations from China alone. In cases 7 and 8, the PM₁₀ observations above 50 and 100 $\mu\text{g m}^{-3}$ from China, Korea, and Japan are used, respectively. Although the a posteriori emissions for each case differ slightly, the contributions of each source region in the a posteriori dust emissions show a

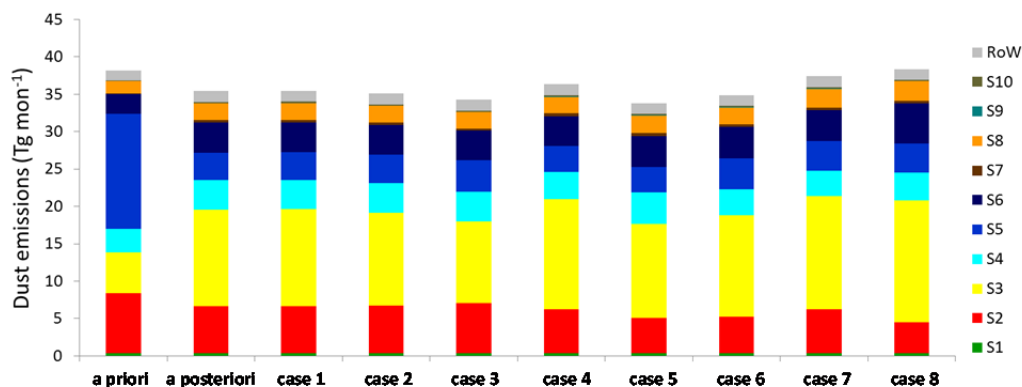


Figure 4.7. Estimates of dust emissions for each source region from inverse modeling analyses. Values with a priori source are forward model results and a posteriori is the best estimates in this study. Each case shows the sensitivity results using different errors and data selections. Cases 1 and 2 show results with 1% and 50% instrumental errors, respectively, and cases 3 and 4 are derived with 150% and 250% errors, respectively, for dust sources using all PM₁₀ observations from China, Korea, and Japan. Case 5 is the result from assigning different transport errors of 100%, 30%, and 70% for China, Korea, and Japan. Cases 6–8 are obtained with 200% dust source errors and 93% transport error and with different data selections. The data for case 6 include the PM₁₀ observations from China alone. In cases 7 and 8, the PM₁₀ observations above 50 $\mu\text{g m}^{-3}$ and 100 $\mu\text{g m}^{-3}$, respectively, from China, Korea, and Japan are used.

consistent change when compared with the a priori sources, indicating the robustness in this inverse model analysis.

CHAPTER V

Comparative inverse analysis of MODIS AODs and PM₁₀ observations to estimate dust emissions during the period 2

The inverse modeling analyses to estimate optimized dust emissions using ground-based PM₁₀ observations and space-based satellite AOD measurements are presented in this chapter. The a priori dust sources discussed in section 3.2, yield 71 Tg over Asia (10–60°N, 70–150°E) in May 2007. As shown in the upper panel of Fig. 5.1, the most dominant source region is the southern area of the Gobi Desert (S5), contributing ~30% of the total dust emission, followed by the Taklamakan Desert (S3) and Mongolia (S2), which account for 25% and 22%, respectively. The inverse modeling results are analyzed focusing on these dominant source regions. Changes in the individual source regions are summarized in Table 5.1 and the results with constrained dust emission estimates from the inverse models are evaluated by comparing with independent observations that are not used in the inverse analysis.

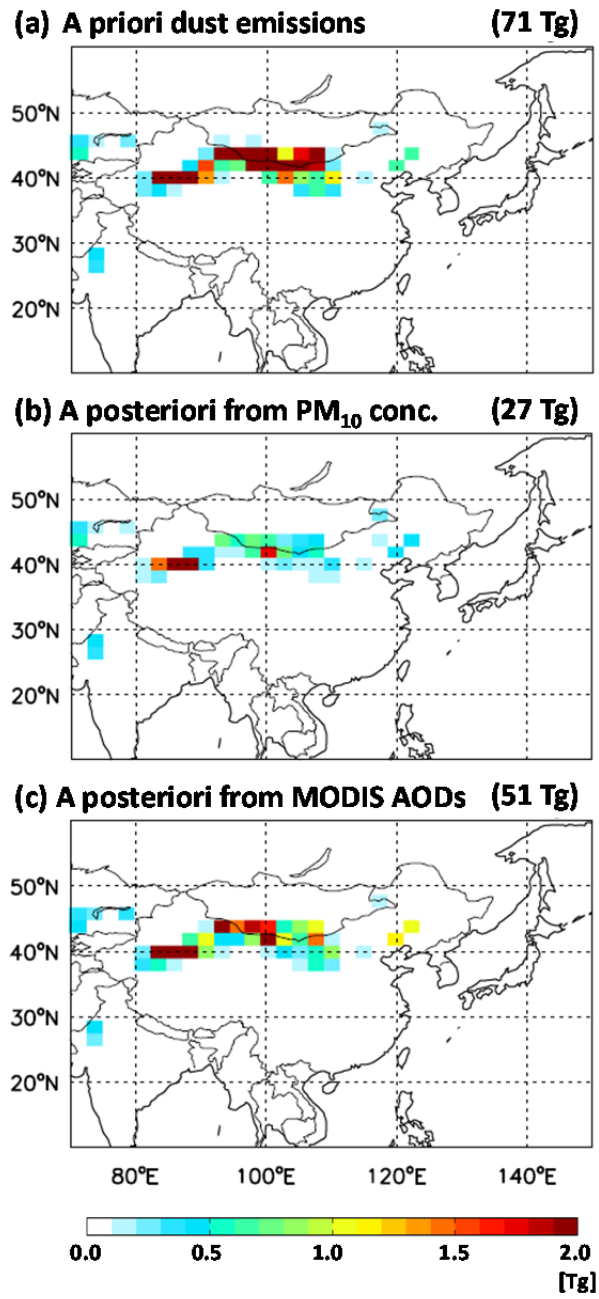


Figure 5.1. Simulated dust emissions with (a) a priori, (b) a posteriori from PM₁₀ concentrations, and (c) a posteriori from MODIS Deep Blue AODs.

Table 5.1. Inverse modeling analysis of dust sources over East Asia in the domain 10–60°N, 70–150°E for May 2007.

A priori sources (Tg mon ⁻¹)												
Regions	S1	S2	S3	S4	S5	S6	S7	S8	S9	S10	RoW	Total
Emissions	0.40	15.82	17.82	7.92	20.95	4.91	0.25	1.36	0.04	0.15	1.78	71.41
(%)	(0.6)	(22.2)	(25.0)	(11.1)	(29.3)	(6.9)	(0.4)	(1.9)	(0.1)	(0.2)	(2.5)	(100)
A posteriori sources (Tg mon ⁻¹)												
Regions	S1	S2	S3	S4	S5	S6	S7	S8	S9	S10	RoW	Total
Emissions from PM ₁₀	0.30	2.99	12.80	1.85	4.25	1.38	0.44	0.88	0.06	0.19	1.81	26.96
(%)	(1.1)	(11.1)	(47.5)	(6.9)	(15.8)	(5.1)	(1.6)	(3.3)	(0.2)	(0.7)	(6.7)	(100)
Emissions from AODs	0.63	7.71	23.93	5.02	6.03	3.86	0.34	2.21	0.04	0.15	1.48	51.40
(%)	(1.2)	(15.0)	(46.6)	(9.8)	(11.7)	(7.5)	(0.7)	(4.3)	(0.1)	(0.3)	(2.9)	(100)
Ratios (a posteriori/a priori)												
Regions	S1	S2	S3	S4	S5	S6	S7	S8	S9	S10	RoW	
Ratios From PM ₁₀	0.8	0.2	0.7	0.2	0.2	0.3	1.8	0.7	1.3	1.3	1.0	
Ratios From AODs	1.6	0.5	1.3	0.6	0.3	0.8	1.3	1.6	1.0	1.0	0.8	

In the following sections, detailed characterization and evaluations of the model with a posteriori dust sources from the PM_{10} observations and from the MODIS Deep Blue AOD measurements are presented, and the robustness of the inverse model and some limitations of different observations used for the optimization of dust emissions are examined.

5.1. A posteriori dust sources from PM₁₀ observations

The a posteriori dust emission from the daily mean PM₁₀ observations is 27 Tg, much lower than a priori value and the spatial distribution of dust emission is altered as shown in the middle panel of Fig. 5.1. The a posteriori dust emissions in Mongolia (S2) and the southern area of the Gobi Desert (S5) decrease by 80% relative to the a priori emissions and account for 11% and 16% respectively to the overall dust emissions. Over the Taklamakan Desert (S3), the a posteriori dust source also decreases by 30% compared to the a priori source and becomes the most dominant source accounting for 48% of the total dust emissions.

The middle panels of Fig. 5.2 show comparisons of the observed versus simulated PM₁₀ concentrations with the a posteriori dust sources constrained using the PM₁₀ observations. The large bias with the a priori dust sources during the dust events (23–31 May) is significantly reduced and the model shows better agreement with the observations. During the whole month, the mean bias of PM₁₀ mass concentrations decreases from 140% to 51% in China. For downwind regions, their mean biases decrease from 130% to 34% in Korea and from 111% to 44% in Japan. This improvement is largely due to the decreased dust emissions from Mongolia and the southern area of the Gobi Desert.

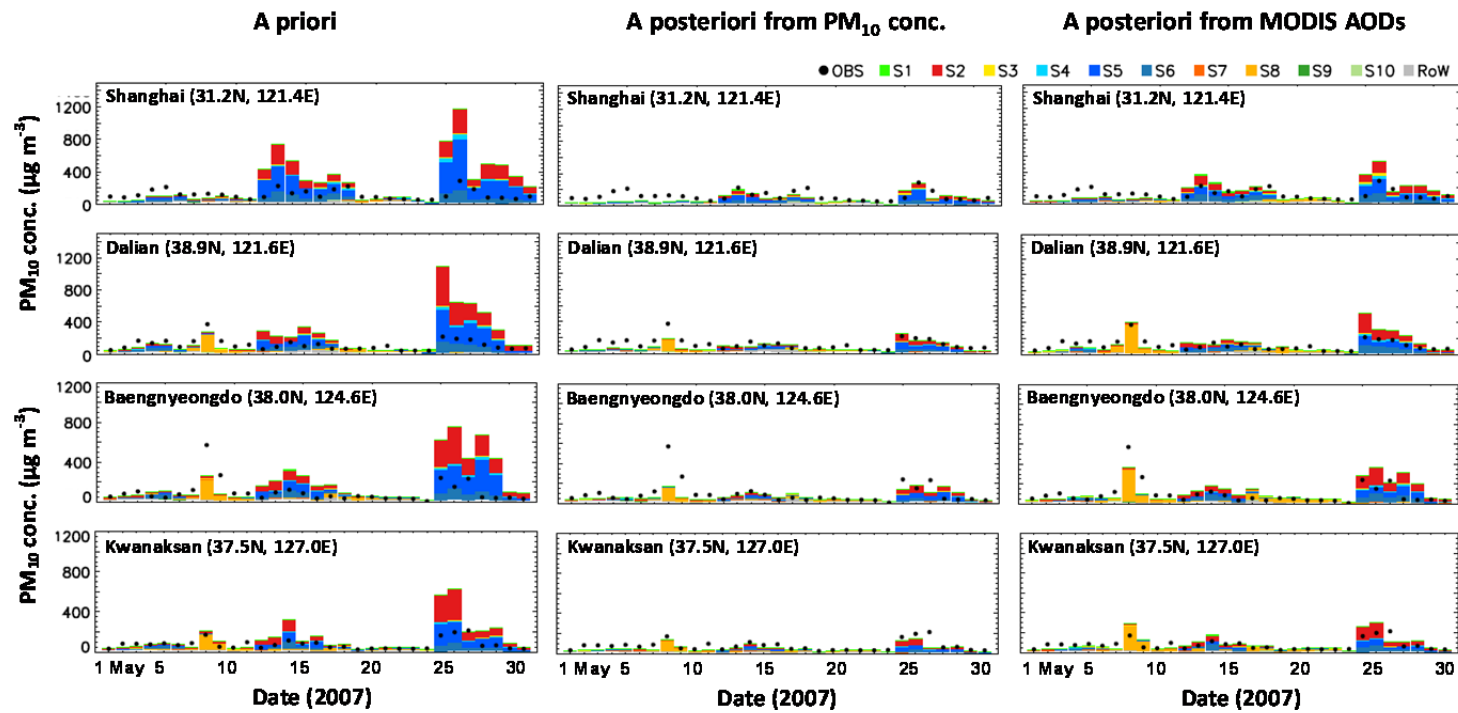


Figure 5.2. Observed daily PM_{10} concentrations versus modeled PM_{10} concentrations with the a priori emissions (left), the a posteriori emissions from the PM_{10} observations (middle), and the a posteriori emissions from the MODIS Deep Blue AODs (right) at Shanghai and Dalian in China, Baengnyeongdo and Kwanaksan in Korea for May 2007.

Furthermore the regression slopes between the observed PM_{10} concentrations and the simulated PM_{10} concentrations with the a posteriori dust sources from the inverse analysis with PM_{10} observations become closer to the unity, and the correlation coefficients are improved as shown in the lower panels of Fig. 5.3.

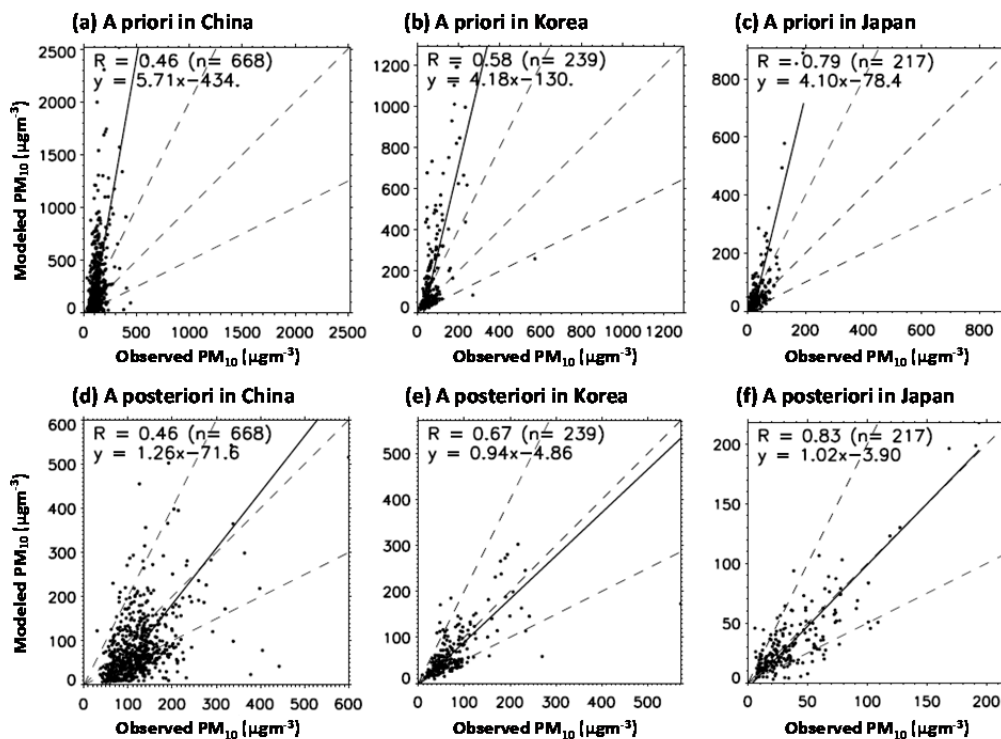


Figure 5.3. Scatterplots of the observed versus simulated PM₁₀ mass concentrations with (a-c) a priori dust sources and with (d-f) a posteriori dust sources from the PM₁₀ observations at China, Korea, and Japan in May 2007.

5.2. Comparative analysis of a posteriori dust sources from MODIS AODs

Another inverse modeling analysis is conducted using daily MODIS Deep Blue AODs. For this analysis, AODs data in the dust source regions from S1 to S8 are used for minimization of the effect of non-dust aerosols on the inversion because the observed AODs in Eastern China (S9 and S10) are generally higher than the model due to non-dust aerosols. This low bias in the model erroneously results in higher a posteriori dust emission from the inverse model despite the use of separate state vector for non-dust aerosols because contributions of dust versus non-dust aerosols to observed AODs are difficult to discern.

The inverse modeling with the MODIS AODs yields a posteriori dust emission of 51 Tg that is lower than the a priori but is almost two times larger than the a posteriori dust emission from the inverse model with the PM₁₀ observations. The lower panel of Fig. 5.1 shows the a posteriori dust emissions from the inverse model with the MODIS AODs. The a posteriori dust emissions in Mongolia (S2) and the southern region of the Gobi Desert (S5) decrease by 50% and 70% respectively compared to the a priori sources and they account for 15% and 12% respectively to the overall dust emissions. The inverse modeling results with the MODIS AODs and the PM₁₀ observations consistently indicate that the

a posteriori dust emissions should decrease in Mongolia (S2) and the southern region of the Gobi Desert (S5). As a result, the previous described large bias with a priori sources becomes reduced during 25 to 29 May. Consistently several comparative studies (Hara et al., 2009; Uno et al., 2008) on dust events for these periods previously reported that dust emissions in the Gobi Desert estimated with assimilation were less than those without assimilation in the May 4-13 and May 21-30 events.

Nevertheless simulated PM_{10} concentrations with the a posteriori sources with the MODIS AODs are still higher than the observations in China because of the excessive dust emissions from Mongolia and the Gobi Desert as shown in right panels of Fig. 5.2. The a posteriori dust emissions with the MODIS AODs are less suppressed than those with the PM_{10} observations in these source regions. These errors may be due to two possible reasons.

One is that a low bias might be attributed to underestimate of fine particle aerosols in the model. Although the MODIS AODs data in deserts and semi-arid regions are selected to minimize the effect of non-dust aerosols on constraints of dust sources, a low bias of the model cannot be completely eliminated. Because the aerosols over the semi-arid region in Northwestern China not only contain natural dust transported from the source regions, but also include local anthropogenic aerosols such as agricultural dust, industrial black carbon and

other anthropogenic aerosols. Huang et al. (2010a) presents that the mean spring AOD derived from MODIS over the semi-arid region in Northwestern China is 0.27, which is 47% higher than that over the semi-arid region in the United States and indicates that the transported natural dust accounts for 53% of this difference. A contribution of the low bias due to underestimation of fine particle aerosols in the model is amplified in AODs rather than in PM₁₀ mass concentrations because particulate matters of 1 μm diameter or smaller (PM₁) have relatively large scattering efficiency.

The other possible reason is the spherical assumption of the non-spherical dust aerosol particles in the model whereas the operational Deep Blue retrievals take into account the non-spherical effect of dust aerosol particles on aerosol property retrieval by using empirical phase functions (Hsu et al., 2004). Additionally, Feng et al. (2009) indicates that the non-spherical effect of dust aerosol particles cannot be neglected for the retrieval of dust AOD because in the case of large AOD (>1), neglecting non-spherical dust aerosol particles may underestimate AOD by as much as 20%. Thus the spherical assumption of the non-spherical dust aerosol particles in the model leads to underestimation of AODs for dust aerosols that causes less suppression of excessive dust emissions in Mongolia and the Gobi Desert.

Whereas during 8-9 May when dust outbreak occurred in Manchuria (S8), the model with the a posteriori sources from the MODIS AODs shows better agreement with the observations compared to that with the a posteriori sources from PM₁₀ observations in the southward downwind regions as shown in Fig. 5.2. This better agreement is attributed to the 60% increase of dust emissions in Manchuria constrained using the MODIS AODs that is a contrary result to the a posteriori dust emissions from PM₁₀ observations. Since only few PM₁₀ observation sites are influenced by dust outbreaks occurred in Manchuria for May 2007 and dust emission in Manchuria is relatively small accounting for below 2% to the overall dust emission in East Asia.

Over the Taklamakan Desert (S3), the a posteriori dust emission increases by 30% and becomes the most dominant source alike the above result accounting for 47% of the total dust emissions. This result is as well a contrast to the a posteriori dust emission from PM₁₀ observations that decreases by 30% in the Taklamakan Desert. It has some limitations to constrain dust sources in the Taklamakan Desert using exclusively PM₁₀ observations. One reason is that PM₁₀ observation sites are mainly located in downwind regions that are far from the Taklamakan Desert thus observed PM₁₀ concentrations are hardly influenced by dust emissions from the Taklamakan Desert. Even though dust aerosols from the Taklamakan Desert are long-range transported to the far downwind regions,

they mainly exist in the free troposphere and their effect on PM_{10} concentrations in the surface air is weak in the downwind regions (Iwasaka et al., 2004; Yamada et al., 2005). Likewise, in May 2007 (period 2) effects of the Taklamakan Desert are relatively small and thus it is difficult to constrain dust emissions in the Taklamakan Desert using PM_{10} observations in downwind regions. Whereas, the PM_{10} observations could constrain dust emissions in the Taklamakan Desert in cases where dust aerosols from the Taklamakan Desert affected the PM_{10} concentrations in the downwind regions significantly such as in April 2001 (period 1).

Fig. 5.4 shows mean biases of the forward model with the a priori dust sources and the a posteriori dust sources from inverse model analyses using the PM_{10} observations and the MODIS AODs. The bias is defined as the mean difference between simulated and observed AODs averaged in May 2007. The largest model bias is located in the southern part of the Gobi Desert and it is reduced more effectively with the a posteriori sources from the PM_{10} observations than those from the MODIS Deep Blue AOD measurements. While a low bias of the model with the a posteriori sources from the PM_{10} observations increases slightly in the Taklamakan Desert as the a posteriori dust emissions decrease in this source region.

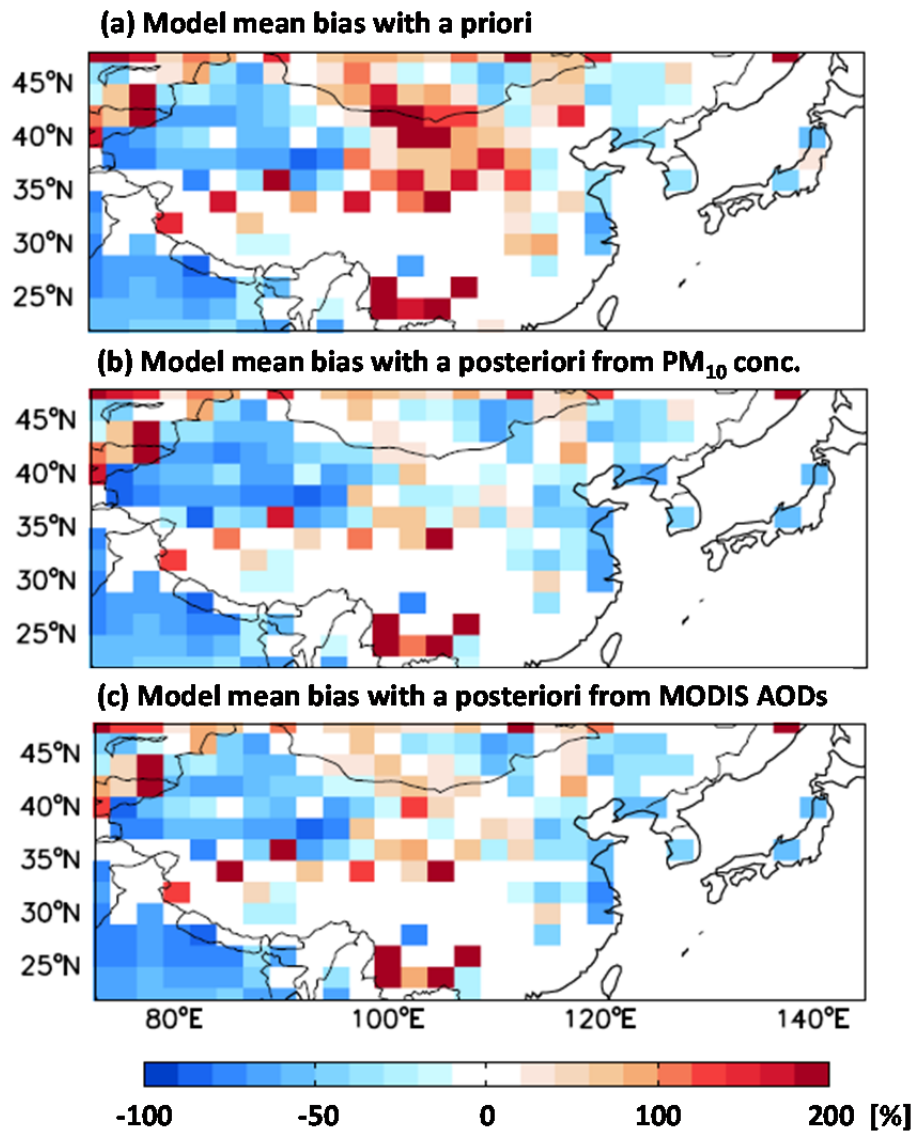


Figure 5.4. GEOS-Chem model mean bias in the simulation of AODs with (a) a priori sources, (b) a posteriori sources from the PM₁₀ concentrations, and (c) a posteriori sources from the MODIS Deep Blue AODs. The bias is defined as the mean of the difference between simulated and observed AODs averaged in May 2007.

To evaluate the optimized dust sources independently, UV Aerosol Index (AI) from the Ozone Monitoring Instrument (OMI) on board the NASA AURA satellite is used. The OMI AI is sensitive to a range of UV absorbing aerosols such as mineral dust, volcanic ash, and black carbon under both cloudless and cloudy conditions and the UV surface reflectivity is typically low which allows OMI to detect aerosols over both land and ocean (Torres et al., 2007). Fig 5.5 presents the monthly mean OMI AI with the simulated column concentrations of dust and black carbon aerosols in May 2007. The model results are sampled at 00-07 UTC for the satellite overpass time when the observations are available in East Asia. Horizontal resolutions of OMI AI and model simulations are $1^{\circ}\times 1^{\circ}$ and $2^{\circ}\times 2.5^{\circ}$, respectively. The highest OMI AI is found in the Taklamakan Desert and its value is generally large over the deserts in India, the Gobi Desert and Inner Mongolia. The simulated column concentrations with the a priori sources show extremely high in the Gobi Desert as well as in the Taklamakan Desert, while the simulated column concentrations with the a posteriori sources present more similar spatial pattern with OMI AI relative to the a priori simulations.

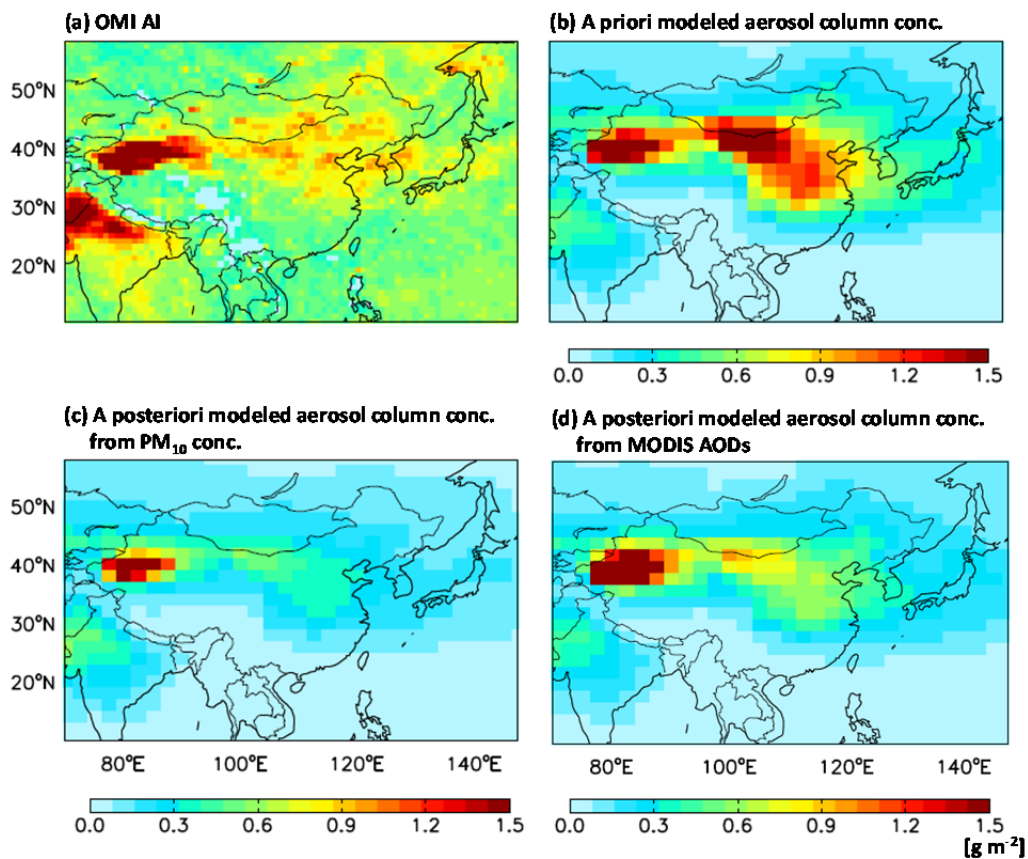


Figure 5.5. Monthly mean UV Aerosol Index (AI) from the Ozone Monitoring Instrument (OMI) versus modeled column concentrations of black carbon and dust aerosols with the a priori and a posteriori dust sources from the PM₁₀ observations and the MODIS Deep Blue AOD measurements in May 2007. The horizontal resolutions of TOMS AI and model simulations are 1°×1° and 2°×2.5°, respectively. Note the difference in color scales.

Furthermore, several analyses are conducted using different data sets to examine the sensitivity of the a posteriori sources to the selection of MODIS Deep Blue AOD measurements data. Fig. 5.6 shows a comparison between the a priori dust sources and the a posteriori dust sources from sensitivity analyses. In this study, the MODIS Deep Blue AOD measurements only in dust source regions from S1 to S8 are used to reduce a bias of AODs due to non-dust aerosols. The data for cases 1-3 include the MODIS Deep Blue AOD measurements in the dust source regions from S1 to S9, from S1 to S10, and in the domain 21-51°N, 71-146°E including downwind regions as well as source regions, respectively. Among the dust source regions, S9 and S10 regions are historical deposition areas where dust emission amounts are relatively small and under the influence of non-dust aerosols as well. In Mongolia (S2), the Taklamakan Desert (S3), the Tsaidam basin and the Kumutage Desert (S4), the a posteriori dust emissions in each case differ slightly because those are located relatively far from S9 and S10 regions. While the a posteriori dust sources in the Gobi Desert (S5), the Mu Us and Hobq deserts (S6) bordered on the historical deposition area (S9) show a considerable difference between the cases. For the data including S10 region, the a posteriori dust sources in the Gobi Desert (S5) less decrease comparing with those for the data excluding S10 region because where the model AODs have a low bias mainly due to the underestimation of

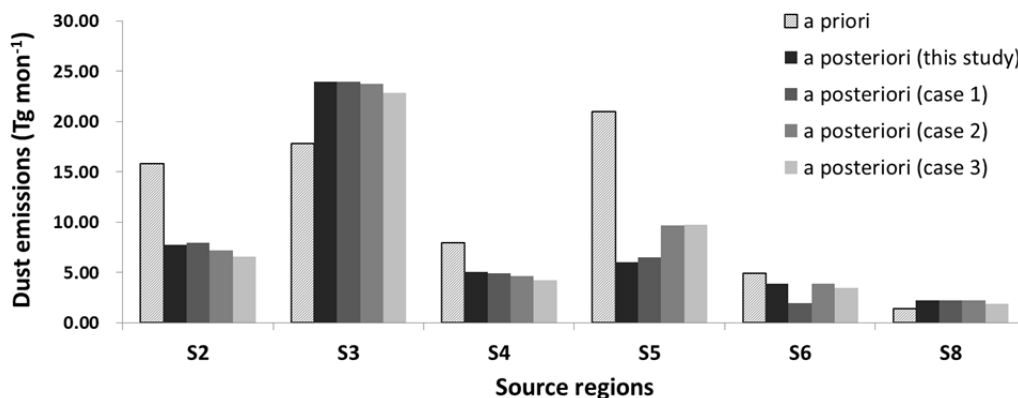


Figure 5.6. Estimates of dust emissions for the dominant individual source regions (S2-S6, S8) from the inverse modeling analyses. Values with the a priori sources are the forward model results and those with the a posteriori sources are the optimized estimates from the MODIS Deep Blue AOD measurements. Each case shows sensitivity results using different data selections. This study uses the MODIS Deep Blue AODs data only in the source regions from S1 to S8. Case 1-3 include the MODIS Deep Blue AODs data in the source regions from S1 to S9, from S1 to S10, and in the domain 21-51°N, 71-146°E including downwind regions as well as source regions, respectively.

non-dust aerosols. However the contributions of each source region in the a posteriori dust emissions show a consistent change when compared with the a priori sources, indicating the robustness in the inverse model analysis.

CHAPTER VI

Improvement of dust emission simulations in the model

The resulting inverse modeling analysis indicates consistently that the a priori dust emissions from Mongolia (S2) and the southern part of the Gobi Desert (S5) should decrease and those from Inner Mongolia (S7) increase. Based on this inverse modeling analysis, some strategies for the improvement of dust emission estimates in the model can be suggested.

First, a clay mass fraction is related to the threshold friction velocity which determines dust mobilization (Fécan et al., 1999) and further the vertical dust flux increases very sensitively with the clay mass fraction in the model (Marticorena and Bergametti, 1995). The left panel of Fig. 6.1 shows vertical dust flux as a function of threshold velocity for different clay content from 0.1 to 0.3. However the DEAD scheme expresses the sandblasting simply as a function of the mass fraction of clay particles in the parent soil and the clay fraction is assumed to be constant leading to a dust emission rate proportional to the saltation flux alone (Zender et al., 2003). In the model, the mass fraction of clay particles is globally fixed to 0.2 (sandy loam) that leads to mobilize too much

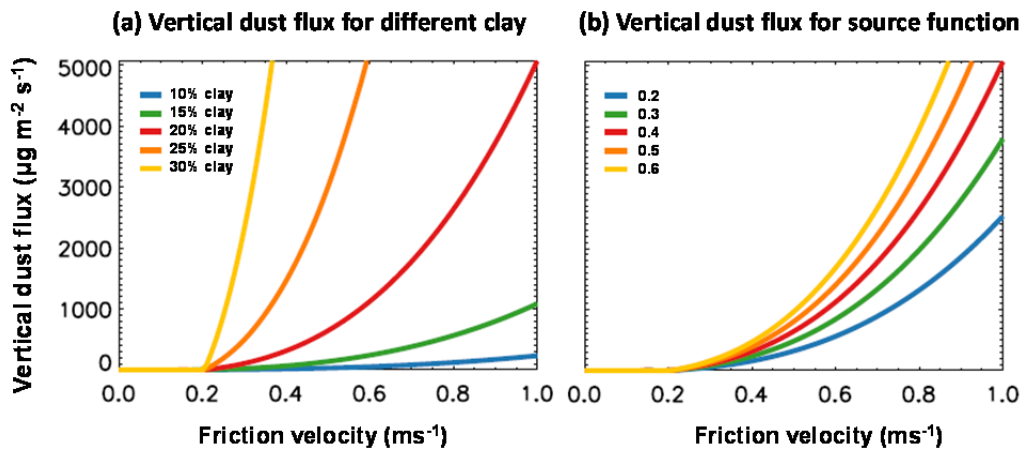


Figure 6.1. Vertical dust flux as a function of friction velocity (a) for the different clay mass fraction from 0.1 to 0.3 and (b) for the source function from 0.2 to 0.6 in the model.

dust emissions in the Gobi Desert such as Southern Mongolia and Northern China.

Simulated dust emissions using variable clay mass fractions with 0.2 cap in May 2007 are compared with the a priori and a posteriori dust emissions constrained using ground-based PM_{10} concentrations and MODIS AODs in Fig. 6.2. Here IGBP soil texture data (Global Soil Data Task Group, 2000) are used. As the variable clay mass fractions are used to estimate dust emissions, the distribution of dust emissions is changed to decrease of dust emissions in the Gobi Desert, the Taklamakan Desert and Mongolia. As a result, a spatial distribution of modeled dust emissions using variable clay mass fractions with 0.2 cap becomes similar that of the a posteriori dust emissions. Fig. 6.3 shows scatterplots comparisons of the observed versus simulated PM_{10} concentrations with the a priori dust sources, dust emissions using variable clay mass fractions with 0.2 cap, and the a posteriori dust emissions constrained using PM_{10} concentrations and MODIS AODs over East Asia. The high bias with the a priori dust sources indicated with a regression slope of 4.80 is significantly reduced to that of 1.76 as the variable clay mass fractions are used to estimate dust emissions and the model shows better agreement with the observations.

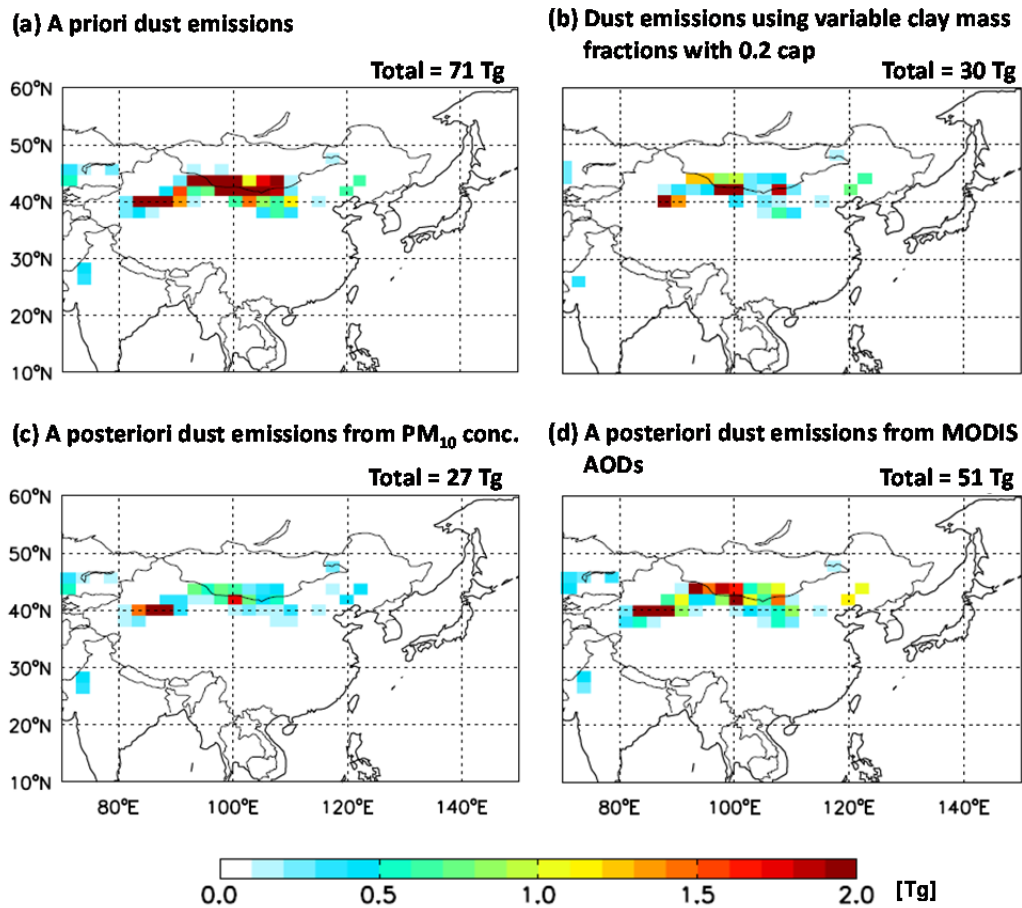


Figure 6.2. Simulated dust emissions with (a) the a priori, (b) using variable clay mass fractions with 0.2 cap, (c) the a posteriori from PM₁₀ concentrations, and (d) the a posteriori from MODIS AODs in May 2007.

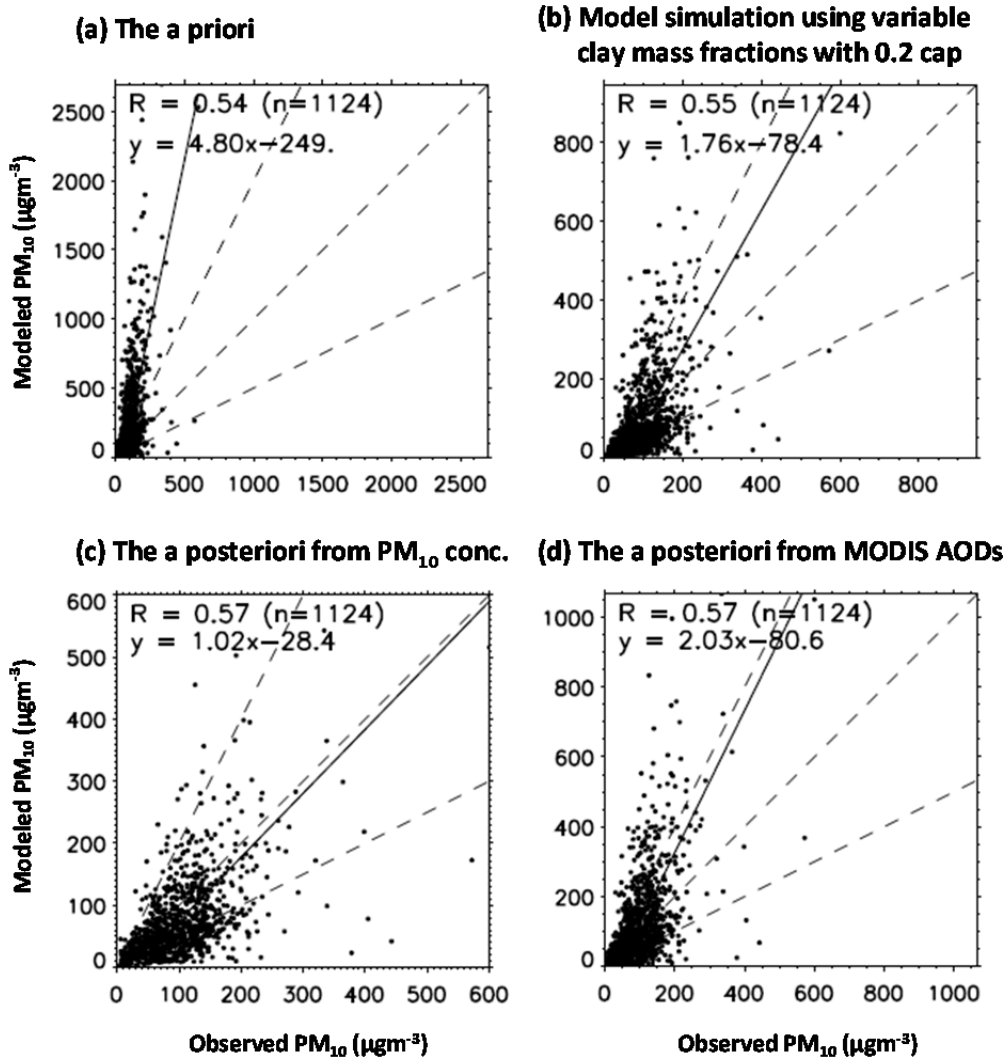


Figure 6.3. Scatterplots of the observed versus simulated PM_{10} mass concentrations with (a) the a priori, (b) using variable clay mass fractions with 0.2 cap, (c) the a posteriori from PM_{10} concentrations, and (d) the a posteriori from MODIS AODs in May 2007.

Second, dust emissions are confined by topographic depressions in desert and semi-arid desert areas of the world (Ginoux et al., 2001) using a source function that replaces the erodibility and the bare land fraction considering vegetation cover in the model. As shown in the right panel of Fig. 6.1, dust emission is proportional to the source function that is time invariant and does not consider vegetation coverage. However the vegetation coverage is a critical factor including seasonal and interannual variations in dust occurrence trends (Zou and Zhai, 2004). For that reason dust emissions over Mongolian Plateau in the growing season are overestimated in the model. Therefore it is important to quantitatively model the effect of vegetation on the dust emission mechanism. Sugimoto et al. (2010) indicates that the threshold surface friction velocity estimated from the results of the data assimilation is different by the vegetation growth data and Park et al. (2010) presents the parameterization of the dust emission reduction factor using Normalized Difference Vegetation Index (NDVI).

Third, the source function might be insufficient to represent the recent extension of dust source regions due to desertification and deforestation of Inner Mongolia and Manchuria. Desert and semi-desert regions that are not included in the U.S. Geological Survey (USGS) land cover data set, have been found between 1990s and 2000s in the satellite data (Hsu et al., 2006). Overall, it is needed to adopt physically based dust mobilization scheme in the model in order

to more quantitatively simulate the effect of land surface conditions including vegetation cover, land cover and soil texture that are critical factors to affect dust mobilization. Rightly those input data should be corrected and updated with using various measurements as well.

CHAPTER VII

Summary and conclusions

An inverse model was applied to obtain optimized a posteriori dust emissions during springtime in East Asia. The inversion was based on the maximum a posteriori Bayesian synthesis method with GEOS-Chem global 3-D chemical transport model (CTM) as the forward model to simulate the PM₁₀ concentrations including non-dust in addition to dust aerosols. This study presented an attempt to apply inverse modeling to soil dust aerosol emissions from different geographical source regions over East Asia, using daily PM₁₀ mass concentrations in the surface air and MODIS Deep Blue AODs because direct dust aerosol observations were very scarce over East Asia.

First, the forward model was evaluated by comparing simulated PM₁₀ mass concentrations to observations in China, Korea, and Japan, focusing on the dust outbreak events in April 2001 (period 1) and May 2007 (period 2). During these dust events, the model was generally higher than the observations near the dust source regions in China, mainly due to the high dust emissions from the Gobi Desert.

For the period 1, the inverse modeling analysis from the ground-based PM₁₀ observations indicated that the a priori dust emissions from the southern part of the Gobi Desert (S5) were too high, while those from the Taklamakan Desert (S3), Eastern Mongolia, and Inner Mongolia (S7) were too low. The resulting a posteriori source in the southern Gobi Desert was 3.7 Tg mon⁻¹, representing a decrease of 76% from the a priori source. Meanwhile, over the Taklamakan Desert (S3), the a posteriori emissions (12.9 Tg mon⁻¹) were two times larger than the a priori emissions and the a posteriori sources in Manchuria (S8) increased by 36% and amounted to 2.2 Tg mon⁻¹. The Manchuria source region is close to the Korean peninsula and the resulting change improved the simulation when compared to the observations in Korea. Over Eastern and Inner Mongolia (S7), the a posteriori sources also increased by a factor of three, but the absolute increase was relatively marginal. Overall, the total simulated dust emissions over East Asia (10–60°N, 70–150°E) decreased only slightly (~7%) from the a priori to the a posteriori sources in April 2001, but improved the spatial pattern of the simulated PM₁₀ concentrations, resulting in a much better agreement with the observations.

For the period 2, the inverse modeling analyses with daily MODIS AODs and PM₁₀ observations in the surface air were used to compare the top-down estimates of soil dust emissions in East Asia. The relative residual error (RRE)

method (Palmer et al., 2003) was used to quantify the observational error variance that was mainly contributed by the forward model error, and instrument and representation errors were relatively small. The errors were highest in the southern region of the Gobi Desert (S5). The inverse modeling analyses with the MODIS AODs and the PM₁₀ observations consistently indicated the decrease of dust emissions in Mongolia (S2) and the southern region of the Gobi Desert (S5). As a result, the large bias with a priori sources during dust events was reduced and the model with a posteriori dust sources presented good agreement with the observations. Nevertheless during 25 to 29 May, the simulated PM₁₀ concentrations with a posteriori sources from the MODIS AODs were still higher than the observations in China due to the excessive dust emissions from Mongolia and the Gobi Desert. These errors might be attributed to a low bias due to underestimation of non-dust aerosols and spherical assumption even for the non-spherical dust aerosols in the model.

Whereas during 8-9 May a dust outbreak occurred in Manchuria (S8), the model with a posteriori from the MODIS AODs showed better agreement with the observations compared to that from PM₁₀ observations as the a posteriori dust emissions from MODIS AODs increase in Manchuria. Over the Taklamakan Desert (S3), the a posteriori dust emission from the MODIS AODs increased, while that from the PM₁₀ observations decreased because the PM₁₀ observation

sites are mainly located in downwind regions that are far from the Taklamakan Desert to be affected by the dust emission from this source region. For this reason, it is difficult to accurately quantify dust emissions in the Taklamakan Desert using exclusively PM₁₀ observations in downwind regions. The inverse modeling analyses using the MODIS AODs and the PM₁₀ observations are appropriate to constrain dust sources only for the periods of dust storm outbreaks when non-dust aerosols are relatively less significant.

Based on the inverse modeling analyses consistently indicating the decrease of dust emissions in Mongolia and the southern region of the Gobi Desert, this study suggested some strategies for the improvement of dust emission estimates in the model. First, the soil characterization for sandblasting should be considered with using the reliable Asian erodible soil data sets and moreover land surface condition such as vegetation cover and land cover should be considered with accurate input data, allowing for improved quantification of the spatial and temporal distributions of dust aerosols and better understanding of air quality and climate change in East Asia.

REFERENCES

- Abdou, W.A., Diner, D.J., Martonchik, J.V., Bruegge, C.J., Kahn, R.A., Gaitley, B.J., Crean, K.A., Remer, L.A., Holben, B., 2005. Comparison of coincident Multiangle Imaging Spectroradiometer and Moderate Resolution Imaging Spectroradiometer aerosol optical depths over land and ocean scenes containing Aerosol Robotic Network sites. *Journal of Geophysical Research* 110, D10S07.
- Andreae, M.O., Merlet, P., 2001. Emission of trace gases and aerosols from biomass burning. *Global Biogeochemical Cycles* 15, 955-966.
- Chin, M., Ginoux, P., Kinne, S., Torres, O., Holben, B.N., Duncan, B.N., Martin, R.V., Logan, J.A., Higurashi, A., Nakajima, T., 2002. Tropospheric Aerosol Optical Thickness from the GOCART Model and Comparisons with Satellite and Sun Photometer Measurements. *Journal of the Atmospheric Sciences* 59, 461-483.
- Chin, M., Ginoux, P., Lucchesi, R., Huebert, B., Weber, R., Anderson, T., Masonis, S., Blomquist, B., Bandy, A., Thornton, D., 2003. A global aerosol model forecast for the ACE-Asia field experiment. *Journal of Geophysical Research* 108, 8654.
- Choi, Y., Park, R.J., Ho, C., 2009. Estimates of ground-level aerosol mass concentrations using a chemical transport model with Moderate Resolution Imaging Spectroradiometer (MODIS) aerosol observations over East Asia. *Journal of Geophysical Research* 114, D04204.
- Chu, D.A., Kaufman, Y.J., Ichoku, C., Remer, L.A., Tanré, D., Holben, B.N., 2002. Validation of MODIS aerosol optical depth retrieval over land. *Geophysical Research Letters* 29, 8007.
- Chu, P.C., Chen, Y., Lu, S., Li, Z., Lu, Y., 2008. Particulate air pollution in Lanzhou China. *Environment International* 34, 698-713.
- Darmenova, K., Sokolik, I.N., Darmenov, A., 2005. Characterization of east Asian dust outbreaks in the spring of 2001 using ground-based and satellite data. *Journal of Geophysical Research* 110, D02204.

- Diner, D.J., Abdou, W.A., Bruegge, C.J., Conel, J.E., Crean, K.A., Gaitley, B.J., Helmlinger, M.C., Kahn, R.A., Martonchik, J.V., Pilorz, S.H., Holben, B.N., 2001. MISR aerosol optical depth retrievals over southern Africa during the SAFARI-2000 dry season campaign. *Geophysical Research Letters* 28, 3127-3130.
- Fécan, F., Marticorena, B., Bergametti, G., 1999. Parametrization of the increase of the aeolian erosion threshold wind friction velocity due to soil moisture for arid and semi-arid areas. *Annales Geophysicae* 17, 149-157.
- Fairlie, T.D., Jacob, D.J., Park, R.J., 2007. The impact of transpacific transport of mineral dust in the United States. *Atmospheric Environment* 41, 1251-1266.
- Feng, Q., Yang, P., Kattawar, G.W., Hsu, C.N., Tsay, S.C., Laszlo, I., 2009. Effects of particle nonsphericity and radiation polarization on retrieving dust properties from MODIS observations. *Journal of Aerosol Science* 40, 776-789.
- Forster, P., Ramaswamy, V., Artaxo, P., Berntsen, T., Betts, R., Fahey, D.W., Haywood, J., Lean, J., Lowe, D.C., Myhre, G., Nganga, J., Prinn, R., Raga, G., Schulz, M., Dorland, R.V., 2007. Changes in Atmospheric Constituents and in Radiative Forcing. *Climate Change 2007: The Physical Science Basis. Contribution of Working Group I to the Fourth Assessment Report of the Intergovernmental Panel on Climate Change*, edited by: Solomon, S., D. Qin, M. Manning, Z. Chen, M. Marquis, K.B. Averyt, M. Tignor and H.L. Miller, Cambridge University Press, Cambridge, United Kingdom and New York, NY, USA.
- Giglio, L., van der Werf, G.R., Randerson, J.T., Collatz, G.J., Kasibhatla, P., 2006. Global estimation of burned area using MODIS active fire observations. *Atmospheric Chemistry and Physics* 6, 957-974.
- Ginoux, P., Chin, M., Tegen, I., Prospero, J.M., Holben, B., Dubovik, O., Lin, S.-J., 2001. Sources and distributions of dust aerosols simulated with the GOCART model. *Journal of Geophysical Research* 106, 20255-20273.
- Goldman, G., Mulholland, J., Strickland, M., Tolbert, P., 2009. Assessment of Ambient Air Pollutant Measurement Error Associated with Instrument Precision and Spatial Heterogeneity. *Epidemiology* 20, S80.

- Gong, D.-Y., Ho, C.-H., Chen, D., Qian, Y., Choi, Y.-S., Kim, J., 2007. Weekly cycle of aerosol-meteorology interaction over China. *Journal of Geophysical Research* 112, D22202.
- Gong, S.L., Zhang, X.Y., Zhao, T.L., McKendry, I.G., Jaffe, D.A., Lu, N.M., 2003. Characterization of soil dust aerosol in China and its transport and distribution during 2001 ACE-Asia: 2. Model simulation and validation. *Journal of Geophysical Research* 108, 4262.
- Group, G.S.D.T., 2000. Global Gridded Surfaces of Selected Soil Characteristics (IGBP-DIS). Oak Ridge National Laboratory Distributed Active Archive Center, Oak Ridge, Tennessee, U.S.A. .
- Hakami, A., Henze, D.K., Seinfeld, J.H., Chai, T., Tang, Y., Carmichael, G.R., Sandu, A., 2005. Adjoint inverse modeling of black carbon during the Asian Pacific Regional Aerosol Characterization Experiment. *Journal of Geophysical Research* 110, D14301.
- Hara, Y., Yumimoto, K., Uno, I., Shimizu, A., Sugimoto, N., Liu, Z., Winker, D.M., 2009. Asian dust outflow in the PBL and free atmosphere retrieved by NASA CALIPSO and an assimilated dust transport model. *Atmospheric Chemistry and Physics* 9, 1227-1239.
- Henze, D.K., Seinfeld, J.H., Shindell, D.T., 2009. Inverse modeling and mapping US air quality influences of inorganic PM_{2.5} precursor emissions using the adjoint of GEOS-Chem. *Atmospheric Chemistry and Physics* 9, 5877-5903.
- Herman, J.R., Bhartia, P.K., Torres, O., Hsu, C., Seftor, C., Celarier, E., 1997. Global distribution of UV-absorbing aerosols from Nimbus 7/TOMS data. *Journal of Geophysical Research* 102, 16911-16922.
- Holben, B.N., Eck, T.F., Slutsker, I., Tanré, D., Buis, J.P., Setzer, A., Vermote, E., Reagan, J.A., Kaufman, Y.J., Nakajima, T., Lavenu, F., Jankowiak, I., Smirnov, A., 1998. AERONET—A Federated Instrument Network and Data Archive for Aerosol Characterization. *Remote Sensing of Environment* 66, 1-16.
- Hsu, N.C., Si-Chee, T., King, M.D., Herman, J.R., 2004. Aerosol properties over bright-reflecting source regions. *IEEE Transactions on Geoscience and Remote Sensing* 42, 557-569.

- Hsu, N.C., Tsay, S.C., King, M.D., Herman, J.R., 2006. Deep Blue retrievals of Asian aerosol properties during ACE-Asia. *IEEE Transactions on Geoscience and Remote Sensing* 44, 3180-3195.
- Huang, J., Minnis, P., Yan, H., Yi, Y., Chen, B., Zhang, L., Ayers, J.K., 2010a. Dust aerosol effect on semi-arid climate over Northwest China detected from A-Train satellite measurements. *Atmospheric Chemistry and Physics* 10, 6863-6872.
- Huang, Q., Cheng, S.Y., Li, Y.P., Li, J.B., Chen, D.S., Wang, H.Y., 2010b. An Integrated MM5-CAMx Modeling Approach for Assessing PM₁₀ Contribution from Different Sources in Beijing, China. *Journal of Environmental Informatics* 15, 47-61.
- Ichoku, C., Remer, L.A., Eck, T.F., 2005. Quantitative evaluation and intercomparison of morning and afternoon Moderate Resolution Imaging Spectroradiometer (MODIS) aerosol measurements from Terra and Aqua. *Journal of Geophysical Research* 110, D10S03.
- Iwasaka, Y., Shi, G.Y., Kim, Y.S., Matsuki, A., Trochkin, D., Zhang, D., Yamada, M., Nagatani, T., Nagatani, M., Shen, Z., Shibata, T., Nakata, H., 2004. Pool of Dust Particles over the Asian Continent: Balloon-borne Optical Particle Counter and Ground-based Lidar Measurements at Dunhuang, China. *Environmental Monitoring and Assessment* 92, 5-24.
- Jacob, D.J., 2007. Lectures on inverse modeling.
- Jaffe, D., Price, H., Parrish, D., Goldstein, A., Harris, J., 2003. Increasing background ozone during spring on the west coast of North America. *Geophysical Research Letters* 30, 1613.
- Jang, Y., Kim, J., Kim, P., Shin, Y., Seo, Y., 2008. A Study on the Estimation of Fugitive PM₁₀ Emission in the Metropolitan Area, Proceeding of the 47th Meeting of KOSAE (2008). Korean Society for Atmospheric Environment, pp. 367-368.
- Jeong, J.I., Park, R.J., Youn, D., 2008. Effects of Siberian forest fires on air quality in East Asia during May 2003 and its climate implication. *Atmospheric Environment* 42, 8910-8922.

- Jickells, T.D., An, Z.S., Andersen, K.K., Baker, A.R., Bergametti, G., Brooks, N., Cao, J.J., Boyd, P.W., Duce, R.A., Hunter, K.A., Kawahata, H., Kubilay, N., laRoche, J., Liss, P.S., Mahowald, N., Prospero, J.M., Ridgwell, A.J., Tegen, I., Torres, R., 2005. Global Iron Connections Between Desert Dust, Ocean Biogeochemistry, and Climate. *Science* 308, 67-71.
- Kiley, C.M., Fuelberg, H.E., Palmer, P.I., Allen, D.J., Carmichael, G.R., Jacob, D.J., Mari, C., Pierce, R.B., Pickering, K.E., Tang, Y., Wild, O., Fairlie, T.D., Logan, J.A., Sachse, G.W., Shaack, T.K., Streets, D.G., 2003. An intercomparison and evaluation of aircraft-derived and simulated CO from seven chemical transport models during the TRACE-P experiment. *Journal of Geophysical Research* 108, 8819.
- Kopacz, M., Jacob, D.J., Henze, D.K., Heald, C.L., Streets, D.G., Zhang, Q., 2009. Comparison of adjoint and analytical Bayesian inversion methods for constraining Asian sources of carbon monoxide using satellite (MOPITT) measurements of CO columns. *Journal of Geophysical Research* 114, D04305.
- Kurosaki, Y., Mikami, M., 2004. Effect of snow cover on threshold wind velocity of dust outbreak. *Geophysical Research Letters* 31, L03106.
- Kwon, H.-J., Cho, S.-H., Chun, Y., Lagarde, F., Pershagen, G., 2002. Effects of the Asian Dust Events on Daily Mortality in Seoul, Korea. *Environmental Research* 90, 1-5.
- Lim, J.-Y., Chun, Y., 2006. The characteristics of Asian dust events in Northeast Asia during the springtime from 1993 to 2004. *Global and Planetary Change* 52, 231-247.
- Liu, H., Jacob, D.J., Bey, I., Yantosca, R.M., 2001. Constraints from ²¹⁰Pb and ⁷Be on wet deposition and transport in a global three-dimensional chemical tracer model driven by assimilated meteorological fields. *Journal of Geophysical Research* 106, 109-112,128.
- Liu, M., Westphal, D.L., Wang, S., Shimizu, A., Sugimoto, N., Zhou, J., Chen, Y., 2003. A high-resolution numerical study of the Asian dust storms of April 2001. *Journal of Geophysical Research* 108, 8653.
- Marticorena, B., Bergametti, G., 1995. Modeling the atmospheric dust cycle: 1. Design of a soil-derived dust emission scheme. *Journal of Geophysical Research* 100, 16415-16430.

- Martonchik, J.V., Diner, D.J., Kahn, R., Gaitley, B., Holben, B.N., 2004. Comparison of MISR and AERONET aerosol optical depths over desert sites. *Geophysical Research Letters* 31, L16102.
- Miller, R.L., Tegen, I., Perlwitz, J., 2004. Surface radiative forcing by soil dust aerosols and the hydrologic cycle. *Journal of Geophysical Research* 109, D04203.
- Palmer, P.I., Jacob, D.J., Jones, D.B.A., Heald, C.L., Yantosca, R.M., Logan, J.A., Sachse, G.W., Streets, D.G., 2003. Inverting for emissions of carbon monoxide from Asia using aircraft observations over the western Pacific. *Journal of Geophysical Research* 108, 8828.
- Park, R.J., Jacob, D.J., Field, B.D., Yantosca, R.M., Chin, M., 2004. Natural and transboundary pollution influences on sulfate-nitrate-ammonium aerosols in the United States: implications for policy. *Journal of Geophysical Research* 109, D15204.
- Park, R.J., Jacob, D.J., Kumar, N., Yantosca, R.M., 2006. Regional visibility statistics in the United States: Natural and transboundary pollution influences, and implications for the Regional Haze Rule. *Atmospheric Environment* 40, 5405-5423.
- Park, S.-U., Choe, A., Lee, E.-H., Park, M.-S., Song, X., 2010. The Asian Dust Aerosol Model 2 (ADAM2) with the use of Normalized Difference Vegetation Index (NDVI) obtained from the Spot4/vegetation data. *Theoretical and Applied Climatology* 101, 191-208.
- Park, S.-U., In, H.-J., 2003. Parameterization of dust emission for the simulation of the yellow sand (Asian dust) event observed in March 2002 in Korea. *Journal of Geophysical Research* 108, 4618.
- Prospero, J.M., 1999. Long-term measurements of the transport of African mineral dust to the southeastern United States: Implications for regional air quality. *Journal of Geophysical Research* 104, 15917-15927.
- Prospero, J.M., Ginoux, P., Torres, O., Nicholson, S.E., Gill, T.E., 2002. Environmental characterization of global sources of atmospheric soil dust identified with the NIMBUS 7 Total Ozone Mapping Spectrometer (TOMS) absorbing aerosol product. *Reviews of Geophysics* 40, 1002.

- Remer, L.A., Kaufman, Y.J., Tanré, D., Mattoo, S., Chu, D.A., Martins, J.V., Li, R.-R., Ichoku, C., Levy, R.C., Kleidman, R.G., Eck, T.F., Vermote, E., Holben, B.N., 2005. The MODIS Aerosol Algorithm, Products, and Validation. *Journal of the Atmospheric Sciences* 62, 947-973.
- Rodgers, C.D., 2000. *Inverse Methods for Atmospheric Sounding: Theory and Practice*, World Sci., Hackensack, N. J.
- Seinfeld, J.H., Carmichael, G.R., Arimoto, R., Conant, W.C., Brechtel, F.J., Bates, T.S., Cahill, T.A., Clarke, A.D., Doherty, S.J., Flatau, P.J., Huebert, B.J., Kim, J., Markowicz, K.M., Quinn, P.K., Russell, L.M., Russell, P.B., Shimizu, A., Shinozuka, Y., Song, C.H., Tang, Y., Uno, I., Vogelmann, A.M., Weber, R.J., Woo, J.-H., Zhang, X.Y., 2004. ACE-ASIA: Regional Climatic and Atmospheric Chemical Effects of Asian Dust and Pollution. *Bulletin of the American Meteorological Society* 85, 367-380.
- Seinfeld, J.H., Pandis, S.N., 1998. *Atmospheric Chemistry and Physics*. Wiley, New York, 1326.
- Sekiyama, T.T., Tanaka, T.Y., Shimizu, A., Miyoshi, T., 2010. Data assimilation of CALIPSO aerosol observations. *Atmospheric Chemistry and Physics* 10, 39-49.
- Sokolik, I.N., Toon, O.B., 1996. Direct radiative forcing by anthropogenic airborne mineral aerosols. *Nature* 381, 681-683.
- Sugimoto, N., Hara, Y., Yumimoto, K., Uno, I., Nishikawa, M., Dulam, J., 2010. Dust Emission Estimated with an Assimilated Dust Transport Model Using Lidar Network Data and Vegetation Growth in the Gobi Desert in Mongolia. *SOLA* 6, 125-128.
- Tanaka, T.Y., Chiba, M., 2006. A numerical study of the contributions of dust source regions to the global dust budget. *Global and Planetary Change* 52, 88-104.
- Tang, J., Xue, Y., Yu, T., Guan, Y., 2005. Aerosol optical thickness determination by exploiting the synergy of TERRA and AQUA MODIS. *Remote Sensing of Environment* 94, 327-334.
- Tegen, I., Fung, I., 1994. Modeling of mineral dust in the atmosphere: Sources, transport, and optical thickness. *Journal of Geophysical Research* 99, 22897-22914.

- Torres, O., Bhartia, P.K., Herman, J.R., Ahmad, Z., Gleason, J., 1998. Derivation of aerosol properties from satellite measurements of backscattered ultraviolet radiation: Theoretical basis. *Journal of Geophysical Research* 103, 17099-17110.
- Torres, O., Tanskanen, A., Veihelmann, B., Ahn, C., Braak, R., Bhartia, P.K., Veefkind, P., Levelt, P., 2007. Aerosols and surface UV products from Ozone Monitoring Instrument observations: An overview. *Journal of Geophysical Research* 112, D24S47.
- Uno, I., Carmichael, G.R., Streets, D.G., Tang, Y., Yienger, J.J., Satake, S., Wang, Z., Woo, J.-H., Guttikunda, S., Uematsu, M., Matsumoto, K., Tanimoto, H., Yoshioka, K., Iida, T., 2003. Regional chemical weather forecasting system CFORS: Model descriptions and analysis of surface observations at Japanese island stations during the ACE-Asia experiment. *Journal of Geophysical Research* 108, 8668.
- Uno, I., Wang, Z., Chiba, M., Chun, Y.S., Gong, S.L., Hara, Y., Jung, E., Lee, S.S., Liu, M., Mikami, M., Music, S., Nickovic, S., Satake, S., Shao, Y., Song, Z., Sugimoto, N., Tanaka, T., Westphal, D.L., 2006. Dust model intercomparison (DMIP) study over Asia: Overview. *Journal of Geophysical Research* 111, D12213.
- Uno, I., Yumimoto, K., Shimizu, A., Hara, Y., Sugimoto, N., Wang, Z., Liu, Z., Winker, D.M., 2008. 3D structure of Asian dust transport revealed by CALIPSO lidar and a 4DVAR dust model. *Geophysical Research Letters* 35, L06803.
- van der Werf, G.R., Randerson, J.T., Giglio, L., Collatz, G.J., Kasibhatla, P.S., Arellano Jr, A.F., 2006. Interannual variability in global biomass burning emissions from 1997 to 2004. *Atmospheric Chemistry and Physics* 6, 3423-3441.
- van Donkelaar, A., Martin, R.V., Levy, R.C., da Silva, A.M., Krzyzanowski, M., Chubarova, N.E., Semutnikova, E., Cohen, A.J., 2011. Satellite-based estimates of ground-level fine particulate matter during extreme events: A case study of the Moscow fires in 2010. *Atmospheric Environment* 45, 6225-6232.
- Wang, J., Xu, X., Henze, D.K., Zeng, J., Ji, Q., Tsay, S.-C., Huang, J., 2012. Top-down estimate of dust emissions through integration of MODIS and MISR

aerosol retrievals with the GEOS-Chem adjoint model. *Geophysical Research Letters* 39, L08802.

- Werner, M., Tegen, I., Harrison, S.P., Kohfeld, K.E., Prentice, I.C., Balkanski, Y., Rodhe, H., Roelandt, C., 2002. Seasonal and interannual variability of the mineral dust cycle under present and glacial climate conditions. *Journal of Geophysical Research* 107, 4744.
- White, B.R., 1979. Soil Transport by Winds on Mars. *Journal of Geophysical Research* 84, 4643-4651.
- Wiscombe, W.J., 1980. Improved Mie scattering algorithms. *Applied Optics* 19, 1505-1509.
- Yamada, M., Iwasaka, Y., Matsuki, A., Trochkin, D., Kim, Y., Zhang, D., Nagatani, T., Shi, G.Y., Nagatani, M., Nakata, H., Shen, Z., Chen, B., Li, G., 2005. Feature of Dust Particles in the Spring Free Troposphere over Dunhuang in Northwestern China: Electron Microscopic Experiments on Individual Particles Collected with a Balloon-borne Impactor. *Water, Air, & Soil Pollution: Focus* 5, 231-250.
- Yumimoto, K., Uno, I., Sugimoto, N., Shimizu, A., Liu, Z., Winker, D.M., 2008. Adjoint inversion modeling of Asian dust emission using lidar observations. *Atmospheric Chemistry and Physics* 8, 2869-2884.
- Zender, C.S., Bian, H., Newman, D., 2003. Mineral Dust Entrainment and Deposition (DEAD) model: Description and 1990s dust climatology. *Journal of Geophysical Research* 108, 4416.
- Zhang, L., Gong, S., Padro, J., Barrie, L., 2001. A size-segregated particle dry deposition scheme for an atmospheric aerosol module. *Atmospheric Environment* 35, 549-560.
- Zhang, L., Jacob, D.J., Kopacz, M., Henze, D.K., Singh, K., Jaffe, D.A., 2009. Intercontinental source attribution of ozone pollution at western U.S. sites using an adjoint method. *Geophysical Research Letters* 36, L11810.
- Zhang, X.Y., Gong, S.L., Shen, Z.X., Mei, F.M., Xi, X.X., Liu, L.C., Zhou, Z.J., Wang, D., Wang, Y.Q., Cheng, Y., 2003a. Characterization of soil dust aerosol in China and its transport and distribution during 2001 ACE-Asia: 1. Network observations. *Journal of Geophysical Research* 108, 4261.

- Zhang, X.Y., Gong, S.L., Zhao, T.L., Arimoto, R., Wang, Y.Q., Zhou, Z.J., 2003b. Sources of Asian dust and role of climate change versus desertification in Asian dust emission. *Geophysical Research Letters* 30, 2272.
- Zhao, T.L., Gong, S.L., Zhang, X.Y., Jaffe, D.A., 2008. Asian dust storm influence on North American ambient PM levels: observational evidence and controlling factors. *Atmospheric Chemistry and Physics* 8, 2717-2728.
- Zou, X.K., Zhai, P.M., 2004. Relationship between vegetation coverage and spring dust storms over northern China. *Journal of Geophysical Research* 109, D03104.

국문 초록

토양 먼지 에어로졸은 대류권 에어로졸 질량 농도 중 가장 큰 부분을 차지하고 있는 에어로졸로서 대기질과 기후에 미치는 영향이 상당히 크다. 먼지 에어로졸이 기후 및 인체 건강에 미치는 영향을 평가하고 이를 대비하기 위해서는 먼지 발원지에서의 모래 폭풍 발생을 정확히 모의하는 것이 매우 중요하다. 몽골 및 중국 고비 지역과 타클라마칸 사막을 포함하는 동아시아는 먼지 에어로졸의 중요한 발원지 중 하나이다. 현존하는 다양한 먼지 에어로졸 모델들은 특히 동아시아에서의 먼지 에어로졸 발생량을 모의하는데 있어서 매우 큰 불확실성을 내포하고 있다. 본 연구에서는 인버스 모델링 기법을 먼지 에어로졸 배출량 모의에 활용함으로써 모델의 불확실성을 감소시키고, 동아시아에서의 최적화된 먼지 에어로졸 배출량을 산정하고자 한다. 대기 중 먼지 에어로졸을 포함하여 입경 $10\ \mu\text{m}$ 이하 미세먼지 (PM_{10})의 질량 농도를 모의하기 위하여 전 지구 3차원 화학수송모델인 지오스캠 (GEOS-Chem)을 포워드 모델로 사용하였으며 2001년 4월 (사례1)과 2007년 5월 (사례2)에 초점을 맞춰 봄철에 대한 미세먼지 (PM_{10})의 질량 농도를 모의하였다. 모델의 모의 결과는 동아시아 지역에서 관측된 지표 부근 일 평균 미세먼지 (PM_{10}) 농도와 모디스 (Moderate Resolution Imaging Spectrometer; MODIS) 에어로졸 광학두께 (Aerosol optical depth; AOD) 관측자료를 이용하여 검증되었다. 또한 위의 관측자료들은 인버스 모델링에 사용되었으며 이를 통해 산출된 위에서 아래로의 (top-down) 먼지 배출량은 다양한 관측자료를 이용하여 비교·검증되었다. 모델

의 오차는 몽골 및 중국 고비 지역에서 가장 크게 나타났으며, 지표 부근 미세먼지 (PM_{10}) 농도와 모드스 에어로졸 광학 두께 (AOD) 관측자료를 이용한 인버스 모델링 분석은 동일하게 이 지역에서의 먼지 배출량을 감소시키는 결과를 나타냈다. 따라서 인버스 모델링을 통한 사후 (a posteriori) 먼지 배출량으로 모의된 결과는 관측치에 훨씬 근사해졌다. 이는 먼지 발원지를 지역적으로 구분하여 인버스 모델링 기법에 적용한 방법이 최적화된 먼지 배출량을 산정하는데 매우 유용함을 보여주고 있다. 반면에 타클라마칸 사막과 만주 지역에서는 미세먼지 (PM_{10}) 농도와 에어로졸 광학 두께 (AOD) 관측자료를 이용한 인버스 모델링 분석 결과가 서로 상이한 결과를 나타냈다. 에어로졸 광학 두께 (AOD) 관측자료를 이용한 결과는 이 지역의 배출량을 증가시켰으며 미세먼지 (PM_{10}) 농도를 이용한 결과는 이 지역의 배출량을 감소시켰다. 이에 따라 본 연구에서는 최적화된 먼지 배출량을 산정하는데 있어서 사용된 각 관측자료의 한계점을 논의하고, 인버스 모델링 분석 결과를 토대로 모델의 먼지 배출량 산정을 향상시키는 방안을 몇 가지 제시한다.

주요어: 인버스 모델링, 먼지 배출량, 화학수송모델, 미세먼지 (PM_{10}) 농도, 에어로졸 광학 두께 (AOD)

학번: 2000-30258